Efficient Gas-Solid Hydrogen Storage under the Hybrid Concept

MDPI

![energies logo]

Article

Designing an AB₂-Type Alloy (TiZr-CrMnMo) for the Hybrid Hydrogen Storage Concept

Julián Puszkiel [1,2,3,*], **José M. Bellosta von Colbe [1]**, **Julian Jepsen [1,4]**, **Sergey V. Mitrokhin [5]**, **Elshad Movlaev [5]**, **Victor Verbetsky [5]** and **Thomas Klassen [1,4]**

[1] Department of System Development, Institute of Materials Research, Helmholtz-Zentrum Geesthacht, Max-Planck-Straße 1, 21502 Geesthacht, Germany; jose.bellostavoncolbe@hzg.de (J.M.B.v.C.); julian.jepsen@hzg.de (J.J.); thomas.klassen@hzg.de (T.K.)

[2] Department of Physicochemistry of Materials, Consejo Nacional de Investigaciones Científicas y Técnicas (CONICET), Bariloche R8402AGP, Argentina

[3] Department of Advanced of Materials, IREC Catalonia Institute for Energy Research, 08930 Barcelona, Spain

[4] Materials Technology, Helmut Schmidt University, Holstenhofweg 85, 22043 Hamburg, Germany

[5] Chemistry Department, Lomonosov Moscow State University, 119992 Moscow, Russia; mitrokhin@hydride.chem.msu.ru (S.V.M.); Movlaev@hydride.chem.msu.ru (E.M.); Verbetsky@hydride.chem.msu.ru (V.V.)

[*] Correspondence: julian.puszkiel@hzg.de or jpuszkiel@irec.cat; Tel.: +49-4152-87-2600; Fax: +49-4152-87-2625

Abstract: The hybrid hydrogen storage method consists of the combination of both solid-state metal hydrides and gas hydrogen storage. This method is regarded as a promising trade-off solution between the already developed high-pressure storage reservoir, utilized in the automobile industry, and solid-state storage through the formation of metal hydrides. Therefore, it is possible to lower the hydrogen pressure and to increase the hydrogen volumetric density. In this work, we design a non-stoichiometric AB₂ C14-Laves alloy composed of $(Ti_{0.9}Zr_{0.1})_{1.25}Cr_{0.85}Mn_{1.1}Mo_{0.05}$. This alloy is synthesized by arc-melting, and the thermodynamic and kinetic behaviors are evaluated in a high-pressure Sieverts apparatus. Proper thermodynamic parameters are obtained in the range of temperature and pressure from 3 to 85 °C and from 15 to 500 bar: $\Delta H_{abs.}$ = 22 ± 1 kJ/mol H₂, $\Delta S_{abs.}$ = 107 ± 2 J/K mol H₂, and $\Delta H_{des.}$ = 24 ± 1 kJ/mol H₂, $\Delta S_{des.}$ = 110 ± 3 J/K mol H₂. The addition of 10 wt.% of expanded natural graphite (ENG) allows the improvement of the heat transfer properties, showing a reversible capacity of about 1.5 wt.%, cycling stability and hydrogenation/dehydrogenation times between 25 to 70 s. The feasibility for the utilization of the designed material in a high-pressure tank is also evaluated, considering practical design parameters.

Keywords: AB₂ alloy; hybrid; compressed hydrogen; metal hydride; hydrogen storage; thermodynamics; kinetics

1. Introduction

More than 18 TW is nowadays the total global energy consumption, and about 80 % are covered by fossil fuels [1,2]. In 2018, the global energy demand increased by 2.3 %, which was the highest increase in a decade [3]. Furthermore, global CO₂ emissions increased to 37.1 Gt., owing to the combustion of fossil fuels in the industrial and mainly transport sectors [4]. Thus, a sustainable alternative to fossil fuels is vital to diminish the CO₂ emissions, which is one of the anthropogenic gases responsible for greenhouse effects. Hydrogen is most promising to balance fluctuations in renewable energy supply and demand (peak shaving), and is favorable in particular as an energy carrier for mobility. The introduction of a worldwide hydrogen supply scheme has been under development, and it poses technological, economic and social issues [5].

One of the main bottlenecks for the implementation of a hydrogen infrastructure is the development of systems to safely and efficiently store hydrogen for mobile applications. In this regard, hydrogen has notably lower volumetric energy density (0.003 kWh/L) than liquid hydrocarbons (10.5 kWh/L) at room temperature and 1 bar [6], and this limits the cruising range of a fuel cell-driven vehicle. High pressure and liquid storage are at present the most common methods to store hydrogen. On the one hand, high pressure H_2 storage (350 and 700 bar) presents relatively low volumetric hydrogen density: 20 kg H_2/m^3 for 5 kg H_2 under 350 bar. On the other hand, liquid H_2 storage requires complex and expensive reservoir design because of extremely low operative temperature to avoid the boil-off losses. These limitations have constrained the range of applications for hydrogen as an energy vector [7]. The design of compact hydrogen storage vessels working at relatively low pressures, moderate temperatures and providing high volumetric capacity for the broad commercialization of fuel cell vehicles in our society is one of the most ambitious technological challenges. Storing hydrogen as a hydride compound is an alternative under intensive investigation, which can ease the design of compact hydrogen storage systems [8–10]. Hydride materials can be generally classified as interstitial hydrides, chemically bonded hydrides (binary and complex hydrides) and reactive hydride composites (RHC), in which two hydrides exothermically form a new compound that partially compensates for the endothermic heat upon hydrogen release. One of the main advantage of hydride materials is their high volumetric hydrogen density (MgH_2: 110 kg H_2/m^3, $LaNi_5H_6$ ~ 100 kg H_2/m^3, Mg_2FeH_6: 150 kg H_2/m^3) under lower pressures and in a wide range of temperatures. There is an extensive list of hydrides materials under exhaustive research which offer quite promising characteristics for hydrogen storage, energy storage and hydrogen compression [8–52].

Interstitial metal hydrides (MH) can work in a range from cryogenic to room temperatures, owing to their low stability, and can store more than 100 kg H_2/m^3. MH, such as AB, AB_2, and AB_5 (in which A and B are two different metals or groups of metals) have the advantage of flexibility in tuning thermodynamics by metal substitution, thus absorbing and desorbing hydrogen under desired temperature and pressure conditions. Despite all these advantages, MH possess low gravimetric hydrogen density ranging between 1 to 3 wt.% H [7–25,28–36,41–46,48–56].

In order to overcome the main constraints of the compressed hydrogen storage method (low volumetric hydrogen density) and the MH storage method (low gravimetric hydrogen density), Takeichi et al. [53] proposed the "hybrid hydrogen storage system". This concept consists of the combination of a lightweight high-pressure reservoir (for up to 350 bar) and a solid-state MH system (H_2 absorbing alloy). The hybrid hydrogen storage system presented improved gravimetric and volumetric hydrogen densities as well as a good dynamic response over the individual compressed hydrogen and MH systems [10,54–56].

For the development of the hybrid concept, hydride forming alloys with high desorption plateau pressure, low operative temperature and consequently, small reaction enthalpy, as well as high hydrogen volumetric and gravimetric capacity, are desired: from cryogenic to room temperature and ΔH of about 20 kJ/mol H_2, and over 1 wt.% of capacity are the requirements in our case. Special attention was put on synthesizing stoichiometric and non-stoichiometric AB_2 C14 Laves phase (hexagonal $MgZn_2$ structure) [15,19,22,25,30,31,34,41,42,45,48], BCC phase alloys [11,16,23,28,35,46] and their C14-BCC phase alloys [14,24,28,31,50,52] to be employed for the hybrid concept. BCC and C14-BCC phase alloys have capacities between 2 and 3 wt.%, relatively good cycling stability, and the equilibrium pressures can be tuned to fulfill the hybrid concept requirements. However, the high cost of V (350 to 400 US$/kg [30]) precludes this kind of hydrogen-absorbing alloy from a scaled-up practical application in a widespread fashion [11,14,16,23,24,28,35,46,50,52]. One of the strategies to lower the cost of V-based BCC alloys is to replace V by FeV (30 US$/kg [30]). However, the obtained alloys showed equilibrium pressures out of the range of the hybrid concept applicability and reduced hydrogen capacities [30,35]. Ti-Cr-Mn-based AB_2 C14 Laves alloys present adequate properties for the hybrid concept: a suitable range of equilibrium pressures, hydrogen capacities, and cycling stability [19,22,25,34,41,45,48]. In addition, the prices of their components are acceptable: Ti: 10–25 US$/kg, Cr: 40 US$/kg and Mn: 3 US$/kg, and even

the use of metals such as of Zr: 50 US$/kg and Fe: 1 US$/kg can be contemplated [30,57]. AB$_2$ C14 Laves phases offer the possibility to design non-stoichiometric alloys with enhanced hydrogen storage properties, owing to the introduction of disorder in the C14 hexagonal structure with modified cell parameters [15,19,22,25,34,41,42,45].

In this work, a non-stoichiometric Ti-Zr-Cr-Mn-Mo alloy with C14 Laves hexagonal structure is designed for its use in the hybrid concept. This alloy is synthesized by arc-melting under an inert atmosphere, and its thermodynamic behavior is characterized in a high-pressure Sieverts apparatus. Expanded natural graphite (ENG) is added by a non-energetic mechanical method. The kinetic behavior of the material is assessed before and after the addition of ENG. The addition of 10 wt.% of ENG allows improving the heat transfer properties, and the material shows a reversible capacity of about 1.5 wt.% in the range of pressure required for a hybrid tank, cycling stability and short hydrogenation and dehydrogenation times in the range between 25 to 70 s in laboratory scale. An analysis of the feasibility of the use of the developed alloy for the hybrid concept is also shown based on the real filling density of the material and practical design parameters. To the best of our knowledge, this is the first time that a thorough study has been done for the design and implementation of a material for a modified hybrid concept.

2. Materials and Methods

2.1. Synthesis and Expanded Natural Graphite (ENG) Addition

The synthesis of the alloy was performed by arc-melting of a mixture of pure metals (Ti, Zr, Cr, Mn and Mo, 99.9 % purity or higher) in a water-cooled copper crucible with unspent tungsten electrode under an inert atmosphere from 1.0 to 1.5 bar. The corresponding amount of metals were weighted to synthesize 2 buttons of about 20 g each. Mn was put in excess because of its high vapor pressure in order to compensate for losses during the melting process. In order to prevent further oxidation of the sample, a Ti-getter was introduced along with the mixture of elements to be melted. The melting process was done three times in order to assure the proper homogenization of the samples. Between each process, the buttons were put upside down and re-melted. Moreover, between each melting process, the oven was flushed with Ar to take the contaminated gas away.

In total, 10 wt.% of expanded natural graphite (ENG, GFG50, average particle size: 50 μm purchased from SGL Carbon Group) was added to the arc-melted alloy after hydrogen cycling. The as-melted alloy was first cycled in hydrogen in order to reduce the particle size, and then, handled and stored in a glove box under a controlled atmosphere (<1 ppm O$_2$ and H$_2$O, MBraun Inert gas-system GmbH) in order to avoid further oxidation of the alloy. The cycled alloy in powder form and 10 wt.% of ENG mixture were introduced in a hermetic glass bottle and sealed inside the glove box. The sealed bottle with the material (alloy + 10 wt.% ENG) was mixed in a roller mixer (MULTI-MIX 10, Balik Anlagentechnik GmbH., Wien, Austria) for 24 h at 60 rpm.

2.2. Phase, Composition, Microstructural and Morphological Characterizations

The arc-melted obtained alloy was characterized via X-Ray Diffraction (XRD) in a DRON-3M diffractometer (CuKα radiation) with a graphite monochromator on the reflected X-ray beam and with scanning electronic microscopy–energy dispersive X-ray (SEM–EDX) on a LEO Supra 50 VP with system Oxford INCA Energy (the resolution of the Si (Li) detector is 129 eV on line Mn Ka 5.894 eV). Three measurements in different broad regions of the samples were performed, and the results are taken as an average with their corresponding error. In order to analyze the characteristics of the crystalline structure of the obtained alloy, Rietveld analysis of the XRD pattern was performed using the RIETAN-2000 software [58].

After hydrogen cycling and ENG addition, the microstructural and morphological characteristics of the phases of the material were characterized by XRD, SEM–EDX mapping and particle size distribution (PSD). The XRD analyses were performed in a Bruker D8 Advance, using Cu-Kα radiation.

The SEM photos and EDX mapping analyses were carried out using a ZEISS AURIGA instrument. For the EDX mapping analyses, powder samples (alloy + 10 wt.% ENG after hydrogen cycling) were dispersed on aluminum sample holders and glued on with a silver solution, which also guaranteed electrical conductivity. For the SEM observation, the powder was dispersed on a carbon sticker mounted on an aluminum sample holder. The EDX mapping analyses were done with three different samples and taking four EDX spectra in different regions of the samples, and the compositional amounts calculated as an average of all the measurements with the corresponding error. The PSD analysis of the alloy + 10 wt.% ENG after hydrogen cycling was done in a Mastersizer 2000 MU device by dispersing the sample in deionized water in an ultrasound bath. Four measurements were carried out, and the results expressed as an average of them.

The loose powder density (thereafter called bulk density) of the alloy after synthesis and hydrogen cycling before adding ENG was determined by a weight-volume method using a defined volume and weighing the mass of the powder that fits the volume without compacting it, and estimating the error by repeating the procedure at least 10 times [59]. The crystalline density, porosity and consequently bulk density of the alloy + 10 wt.% ENG was determined with a pycnometer (AccuPyc II 1340 FoamPyc, Micromeritics) under He. In addition, the bulk density of the alloy + 10 wt.% ENG was also determined by the weight-volume method described above. In order to compare the bulk densities of the alloy +10 wt.% ENG after compaction, a volumetric-compression analysis was also done in a Jolting volumeter (JEL STAV II, J. Engelsmann AG.), using a measuring cylinder of 25 mL and 100 jolts. The measurement was repeated four times and the final value was expressed as an average of them with the corresponding error. In this way, it was possible to compare the bulk density before (pycnometer and weight-volume methods) and after the compaction (called tamped density). Equation (1) describes the relation between the porosity (ε) and the crystalline density ($\rho_{crystalline}$) and the bulk or apparent density (ρ_{bulk}):

$$\varepsilon = 1 - \left(\frac{\rho_{bulk}}{\rho_{crystalline}} \right) \tag{1}$$

2.3. Thermodynamic and Kinetic Characterizations

The thermodynamic behavior of the alloy was characterized in a high-pressure Sieverts apparatus [49]. After the synthesis, the alloy was brittle and was crushed easily into pieces between 2 and 5 mm, to be introduced into the sample holder. An amount of 12 g of sample was introduced into the reactor for the pressure-composition-isotherm (PCIs) measurements and further evaluation of the kinetic hydrogenation behavior. Before starting the PCI measurements, the sample holder was kept under 0.4–1.5 kPa of vacuum (mechanical vacuum pump) for 30 min at room temperature. Then, to assure full activation, the sample was left 48 h under 600 bar H_2 and finally heated up to 300 °C under vacuum for full dehydrogenation. Hydrogenation and dehydrogenation PCI measurements were performed at 3, 23, 58, and 85 °C, setting an equilibrium time of 30 min per point. Absorbed and desorbed hydrogen was calculated applying the Hemmes equation (Equation (2)) to take into account the real gas behavior [60]:

$$\left[\frac{p + a(p)}{V^\alpha} \right] [V - b(p)] = RT \tag{2}$$

where p is the pressure, T is the absolute temperature, V is the volume of the gas, R is the universal gas constant and a and b are the pressure-dependent coefficients. The thermodynamic parameters are determined with the van't Hoff equation (Equation (3)) considering the fugacity:

$$RT \ln\left(f_p \right) = \Delta H_r - T\Delta H_r, \tag{3}$$

where ΔH_r and ΔS_r are the enthalpy and entropy change, and f_p is the fugacity. The following equation (Equation (4)) was used to calculate the fugacity, considering the real molar volume calculated with Equation (2):

$$\mathrm{RT}\ln\left(f_p\right) = \mathrm{RT}\ln(p) - \int_0^p (V_{ideal} - V_{real})dp, \tag{4}$$

where V_{ideal} and V_{real} are the ideal and real molar volumes, respectively. Throughout the manuscript, the fugacity is indicated as "p". The equilibrium pressures are calculated as an average of the experimental points in the plateau regions, considering the error propagation theory to assign an error range [61].

The kinetic behavior for the alloy and the alloy + 10 wt.% ENG was evaluated in a Sieverts device (HERA Hydrogen System) [62]. A sample holder, made of a high thermal conductivity alloy with λ = 230–250 W/m K and with an inserted thermocouple, was utilized to avoid wall effects on the temperature readings that include heat dissipation, and to measure the internal temperature of the metal hydride bed. The sample holder was cooled down/heated up with a cooling fluid circulation system connected to a cooling device Julabo FL1201. Sample amounts of 0.3 and 1.2 g of materials were used for the dynamic measurements. The temperature changes inside the hydride bed were recorded with type K thermocouples connected to a thermocouple data logger TC8, PICO Technology. The absorbed/desorbed hydrogen capacity was calculated based on the van der Waals equation. Measurements were performed in the range of temperature between 5 and 35 °C and pressures from ~1.2 to 170 bar; a mechanical vacuum pump (Leybold Trivac) able to reach < 10 kPa of vacuum was employed. The material composed of the alloy after hydrogen cycling +10 wt.% ENG underwent an activation procedure as follows: 1. Vacuum at room temperature for 30 min; 2. Heating up to 100 °C at a ramp of 10 °C/min, and then, holding the temperature for 30 min; 3. Cooling down quickly until room temperature; 4. Hydrogenation under 100 bar at room temperature for 60 min; 5. Vacuum at 100 °C for 30 min. This procedure was repeated 3 times. The hydrogen capacity was calculated, taking into account the error propagation theory applied to the mentioned above Sieverts device to assign an error band to the final wt.% of H_2, as explained in Reference [61]. The error band is in the range of 0.2 to 0.3 wt.% H_2. Additionally, for each pressure and temperature conditions set used for the hydrogenation and dehydrogenation dynamic measurements, a previous measurement with the empty vessel was performed (blank measurement) in order to subtract the rise/drop in the capacity and temperature owing to the initial rise/drop of pressure at the beginning of the kinetic measurements (Joule–Thomson effect): an example of the curves before and after blank subtraction can be seen in Appendix A. The effect of the rise/drop of pressure upon the hydrogen capacity and internal temperature during the initial stage of the measurement did not change substantially the hydrogen capacity (within 0.2–0.3 wt.% H_2 error band) and the temperature of the hydride bed (small differences).

3. Results

This section shows the results obtained from the microstructural, compositional, morphological, and thermodynamic-kinetic characterizations of the TiZr-CrMnMo alloy after synthesis, expanded natural graphite addition (ENG) and hydrogen interaction. Pressure-composition-isotherm (PCIs) and van't Hoff graphs with the thermodynamic parameters evaluated in a high-pressure Sieverts device are exhibited. The kinetic behaviors before and after the addition of expanded natural graphite (ENG) are displayed, and experiments with large and small amounts of sample are included. Properties such as particle size distribution, bulk density and porosity are compared before and after ENG addition.

3.1. TiZr-CrMnMo Alloy: Synthesis and Hydrogen Storage Properties Under High Pressure

Figure 1 shows the XRD pattern with the corresponding Rietveld analysis and the SEM–EDX results of the alloy after synthesis by arc-melting. As seen in Figure 1a, the obtained TiZr-CrMnMo alloy is an AB_2 C14 Laves phase with hexagonal $MgZn_2$ structure (A metals: Ti and Zr, and B metals: Cr, Mn, and Mo). Figure 1b presents the SEM–EDX analysis of the sample and provides the compositions in wt.% and at.%. There was a small amount of Fe contamination (1.1 wt.%). This contamination might

have come from quite a small amount of Fe present in the starting material and the cutting tool used to prepare the materials to be melted. Taking into account the AB_2 structure and the atomic composition with B to A ratio of 1.6 (B: 2 to A: 1.25), it is possible to express the obtained non-stoichiometric alloy as $(Ti_{0.9}Zr_{0.1})_{1.25}Cr_{0.85}Mn_{1.1}Mo_{0.05}$. A table with the corresponding calculations can be seen in Appendix B.

Figure 2 shows the absorption–desorption PCIs and the van't Hoff plot. The values of the equilibrium pressures measured in a range of temperatures between 3 and 85 °C are between 30 and 248 bar, and between 15 and 173 bar for hydrogenation and dehydrogenation, respectively (Figure 2a,b). Hydrogen capacities in the range of 1.2 wt.% (85 °C) and about 1.5 wt.% (3 °C) are obtained. The hysteresis of the PCIs is quantified by the ratio of the equilibrium pressure for hydrogenation (P_{eq}) over the equilibrium pressure for dehydrogenation at a certain temperature. This ratio is between 1.4 (at 85 °C) and 2.0 (at 3 °C). This ratio is not as important for the intended application in hydrogen storage, as opposed to the case of its usage in compression. Instead, the plateau slope is a parameter that affects the driving force for hydrogen absorption and desorption. The slope can be quantified by the equation $S_f = \ln(P_1/P_2)$, where P_1 and P_2 are extreme turning point pressures of the PCI curves [19]. A perfectly flat plateau provides an $S_f = 0$. On the contrary, taken as criterium P_1 equals two times P_2, the value of $S_f = 0.69$ would be a case of considerable slope in the plateau. In this case, the values of S_f ranges from 0.33 and 0.66 for the hydrogenation ($S_{f(3\,°C)}$: 0.31, $S_{f(23\,°C)}$: 0.41, $S_{f(58\,°C)}$: 0.66 and $S_{f(85\,°C)}$: 0.34), and between 0.35 and 0.56 for dehydrogenation ($S_{f(3\,°C)}$: 0.48, $S_{f(23\,°C)}$: 0.35, $S_{f(58\,°C)}$: 0.56 and $S_{f(85\,°C)}$: 0.54). In Figure 3c, the van't Hoff plot and the obtained values of the thermodynamic parameters for hydrogenation and dehydrogenation are shown. Both hydrogenation and dehydrogenation enthalpies are near the 20 kJ/mol H_2 set as an ideal target for the hybrid concept.
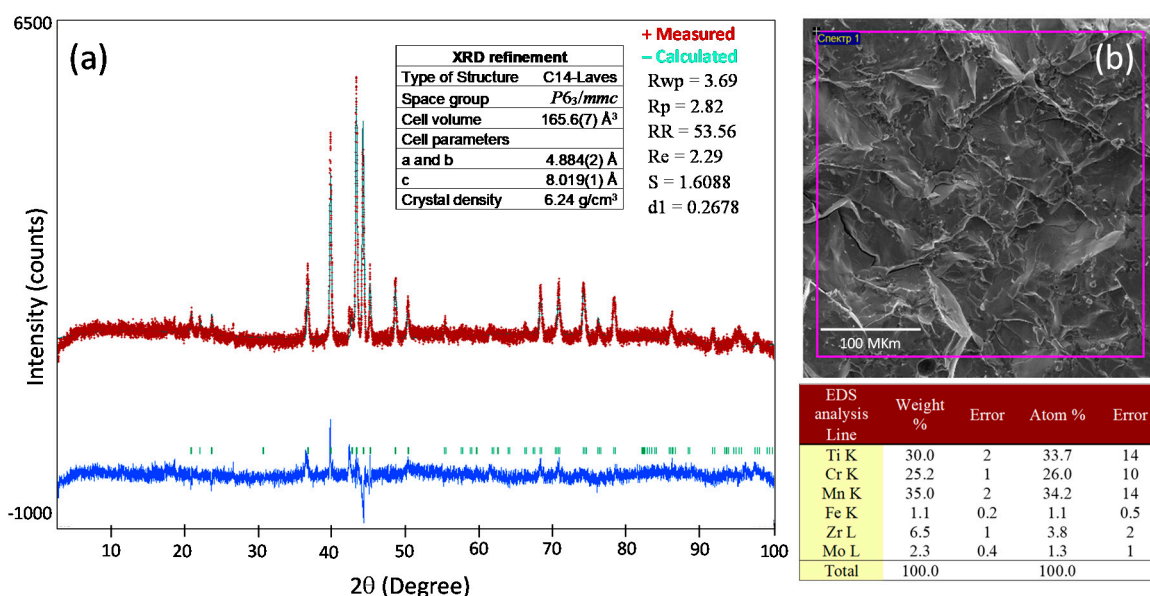

Figure 1. (**a**) XRD analysis and Rietveld refinement, and (**b**) SEM photo of the surface of the TiZr-CrMnMo alloy's button and corresponding EDS after synthesis.

After PCI measurements, a dynamic measurement under extremely high-pressure conditions was carried out as shown in Figure 2d. The volumes of the device did not allow to keep the pressure constant, thus owing to the hydrogen absorption of the sample, the pressure dropped from about 1000 to 150 bar. It is noted that there is a rise of temperature of about 1.5 °C until reaching 90% of the hydrogen capacity, and then, a slightly drop of 0.40 °C until it stabilizes at 23.4 °C. This behavior is related to the heat release upon hydrogenation. Considering that the thermocouple is touching the outer wall of the reactor and the high amount of material, the temperature rise might have been more

significant within the sample itself. Therefore, the equilibrium pressure during this hydrogenation would have been nearby 150 bar, precluding further hydrogenation and reaching a hydrogen capacity slightly over 1.4 wt.%, though in agreement with the hydrogen capacities obtained in the PCIs.
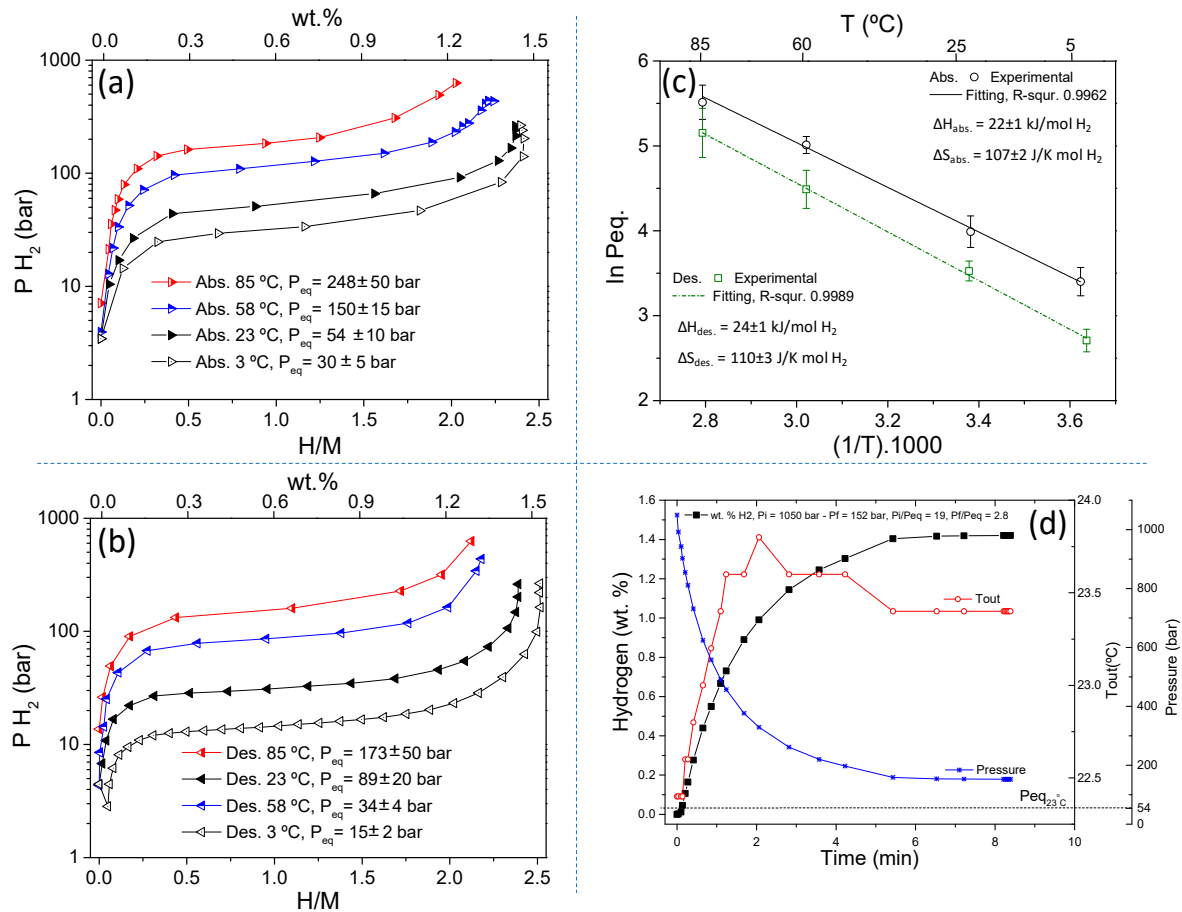

Figure 2. (**a**) Absorption and (**b**) Desorption PCIs with the respective equilibrium pressures at different temperatures, and (**c**) Absorption and desorption van't Hoff plots for the $(Ti_{0.9}Zr_{0.1})_{1.125}Cr_{0.85}Mn_{1.1}Mo_{0.05}$. (**d**) Absorption kinetic behavior under extremely high pressure and after PCI measurements (m = 12 g; high-pressure Sieverts apparatus [49]).

Figure 3 shows the activation and cycling behavior of the $(Ti_{0.9}Zr_{0.1})_{1.25}Cr_{0.85}Mn_{1.1}Mo_{0.05}$ alloy. Without further treatment, the sample slowly absorbed hydrogen till reaching 1.15 wt.% H_2 about 2 h under 80 bar and about 5 °C (Figure 3a). In Figure 3b,c, only the first and last two curves of the cycling are shown. After successive cycling, the material fully absorbs and desorbs hydrogen in about 100 and 150 s, respectively (Figure 3b,c). The hydrogen capacity upon cycling ranges between 1.3 and 1.5 wt.%, with an error band of 0.20–0.30 wt.% calculated from the dehydrogenation with the error propagation theory, as explained in Section 2.3. The discrepancies between the hydrogenation and dehydrogenation capacities of the same cycle are within the error band. There is a difference in hydrogen capacity of about 0.2–0.3 % between the ninth cycle and the other cycles (all cycles not shown presented a hydrogenation and dehydrogenation capacity between 1.1 and 1.3 wt.%). Such a difference might be due to a variation of the temperature in the reference volumes, which can cause a relatively large deviation in the pressure registered in the differential pressure transducer (sensitivity: 0.03 kPa). It is also observed that the temperature measured inside the materials bed notably changes upon hydrogenation and dehydrogenation despite the relatively small amount of sample. In both hydrogenation and dehydrogenation processes, the temperature change is 11 °C.

After hydrogen cycling, the bulk density of the $(Ti_{0.9}Zr_{0.1})_{1.25}Cr_{0.85}Mn_{1.1}Mo_{0.05}$ alloy was determined by the weight-volume method, amounting to 2.878 ± 0.015 g/cm^3. Taking into account the crystalline density determined by XRD (Figure 1A) of 6.24 g/cm^3, the porosity of the material calculated by Equation (1) is 0.54.
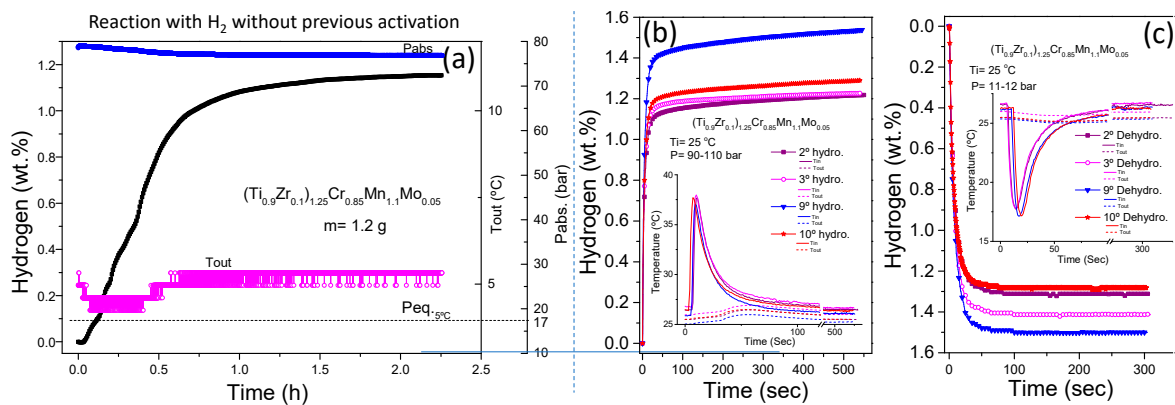

Figure 3. (**a**) First hydrogenation of initial sample after synthesis without previous activation under around 80 bar and 5 °C, and (**b**) hydrogenation and (**c**) dehydrogenation cycling under 90–110 bar and 11–12 bar, respectively, for $(Ti_{0.9}Zr_{0.1})_{1.25}Cr_{0.85}Mn_{1.1}Mo_{0.05}$ (button of alloy broken into pieces by hand with a tool, m = 1.2 g, Sieverts apparatus [62]).

3.2. $(Ti_{0.9}Zr_{0.1})_{1.25}Cr_{0.85}Mn_{1.1}Mo_{0.05}$ with 10 wt.% ENG Added: Characterization, Kinetic-Thermal Behavior and Material's Properties

In order to improve the thermal conductivity [27,63] and to facilitate the expansion of the alloy upon hydrogenation [64,65], 10 wt.% of ENG was added to the alloy after cycling in hydrogen. $(Ti_{0.9}Zr_{0.1})_{1.25}Cr_{0.85}Mn_{1.1}Mo_{0.05}$ + 10 wt.% ENG was mixed for 24 h in an inert atmosphere with a roller mixer. Figure 4a shows the XRD patterns of the $(Ti_{0.9}Zr_{0.1})_{1.25}Cr_{0.85}Mn_{1.1}Mo_{0.05}$ after 10 cycles as described above, as-received ENG and $(Ti_{0.9}Zr_{0.1})_{1.25}Cr_{0.85}Mn_{1.1}Mo_{0.05}$ + 10 wt.% ENG after mixing. The peaks corresponding to the alloy do not exhibit any change, and for the material after mixing, the peaks corresponding to ENG are visible. A Rietveld analysis of the diffraction pattern of the sample after mixing was carried out (not shown). This showed that the mixing process does not have any mechanical effect on the alloy, i.e., strain and stress parameters are not changed. The AB$_2$ lattice parameters and structure are the same as the ones reported in Figure 1a. The parameters of the ENG are: a = 2.60(7) Å, c = 6.69(13) Å, SG P6$_3$/mmc. Figure 4b shows the SEM–EDX mapping of the $(Ti_{0.9}Zr_{0.1})_{1.25}Cr_{0.85}Mn_{1.1}Mo_{0.05}$ + 10 wt.% ENG after mixing and the hydrogen interaction. The weight composition confirms the addition of the 10 wt.% of ENG, and the mapping demonstrates the homogeneous distribution of the elemental composition of the alloy as well as the presence of ENG.

The particle size distribution of the $(Ti_{0.9}Zr_{0.1})_{1.25}Cr_{0.85}Mn_{1.1}Mo_{0.05}$ + 10 wt.% ENG after mixing and the hydrogen interaction was also analyzed via a PSD analyzer and SEM observation (Figure 5). In Figure 5a, it is possible to observe a bimodal particle size distribution. The volume mean diameter (D [3,4]) amounts to 76.8 ± 0.4 μm. Comparing the PSD (Figure 5a) with the SEM images (Figure 5b,c), the smaller particles are taken to belong to the alloy and lay on the first peak in the PSD curve, while the ENG can be associated with the second peak of the PSD curve.
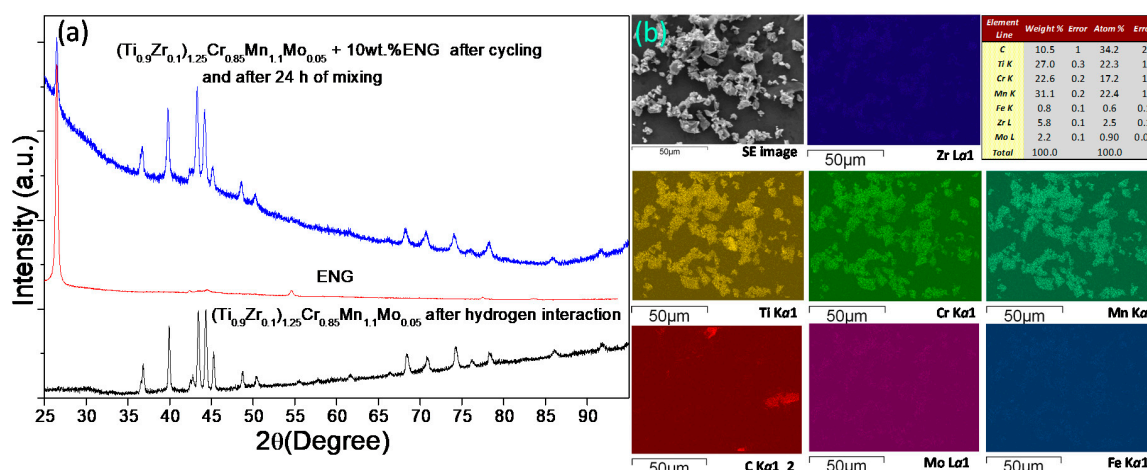
Figure 4. (**a**) XRD of the $(Ti_{0.9}Zr_{0.1})_{1.25}Cr_{0.85}Mn_{1.1}Mo_{0.05}$ + 10 wt.% ENG, ENG and $(Ti_{0.9}Zr_{0.1})_{1.25}Cr_{0.85}Mn_{1.1}Mo_{0.05}$ after hydrogen interaction. (**b**) SEM photo, EDS mapping, and EDS analysis for the $(Ti_{0.9}Zr_{0.1})_{1.25}Cr_{0.85}Mn_{1.1}Mo_{0.05}$ + 10 wt.% ENG in powder form after hydrogen cycling.

Figure 6 shows the first hydrogenation, and then, cycling for the $(Ti_{0.9}Zr_{0.1})_{1.25}Cr_{0.85}Mn_{1.1}Mo_{0.05}$ + 10 wt.% ENG. The sample, as shown in Figure 5b, composed of small alloy particles, did not absorb hydrogen without a previous activation, as it happened with the alloy after synthesis (Figure 3a, which had big particles and without a previous hydrogen interaction). In the beginning, several consecutive hydrogenations under about 100 bar and different temperatures of 5, 10 and 25 °C were performed. The material did not react. Hence, an activation procedure was applied, as described in Section 2.3. After that, the material absorbed hydrogen for the first time under about 100 bar of H_2 at about 25 °C, reaching 1.6 ± 0.20 wt.% H_2 in less than 20 min as shown in Figure 6a. Then, upon cycling, the final capacity is reached in about 25 and 70 s for hydrogenation and dehydrogenation, respectively. The shorter times represent an enhancement in comparison with the alloy without ENG (Figure 3). The hydrogen capacity is between 1.6 and 1.8 wt.%, and it seems to be slightly higher than the one observed for the alloy without ENG. However, the error band calculated from the dehydrogenation and based on the error propagation theory, as explained in Section 2.3, is in the range of 0.20–0.30 wt.%. Hence, the observed capacities overlap (Figures 3 and 6). The addition of ENG leads to a reduction in the temperature rise/drop upon hydrogenation/dehydrogenation, respectively, of about half (~5 °C) of what was observed for the alloy without ENG (Figure 3).

The cycling stability of hydrogen capacity for the $(Ti_{0.9}Zr_{0.1})_{1.25}Cr_{0.85}Mn_{1.1}Mo_{0.05}$ + 10 wt.% ENG was evaluated under a range of temperature and pressures upon 40 cycles as can be seen in Figure 7 (the curves themselves are not shown; the conditions for each cycle are described in detail in Appendix C). This cycling experiments had two aims. First, to verify the dispersion of the hydrogen capacity associated with the errors, which are more pronounced when the kinetic behavior is fast, and the capacities are relatively low as in this case. Second, to verify the stability of the material under different conditions and whether the material suffers a kind of deactivation under the tested conditions. It is not possible to observe a trend towards lower capacity since all values are within the error bars. The average value of all the points with their respective errors from the dehydrogenation experiments amounts to 1.6 ± 0.25 wt.% H_2 with a minimum and maximum range of average values between 1.5 and 1.75 wt.% H_2. Considering all previous experiments carried out in equilibrium and dynamic conditions (Figures 2, 3, 6 and 7), it is reasonable to set a realistic value of the capacity as 1.5 wt.% H_2.
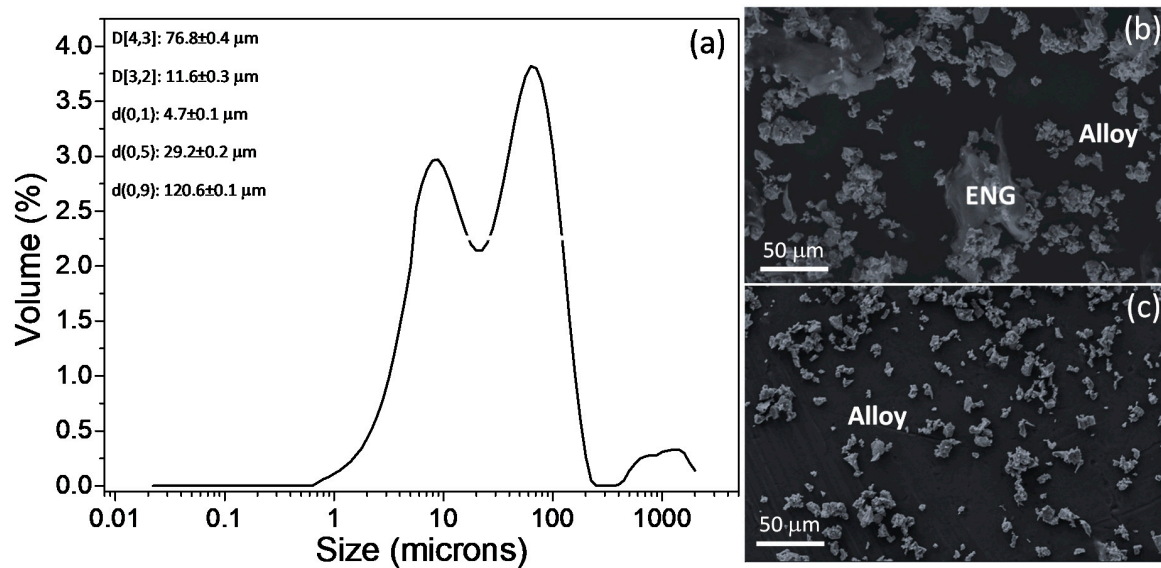
Figure 5. (**a**) PSD analysis and SEM photo for the (**b**) $(Ti_{0.9}Zr_{0.1})_{1.25}Cr_{0.85}Mn_{1.1}Mo_{0.05}$ + 10 wt.% ENG and (**c**) $(Ti_{0.9}Zr_{0.1})_{1.25}Cr_{0.85}Mn_{1.1}Mo_{0.05}$ alloy in powder form after hydrogen cycling.
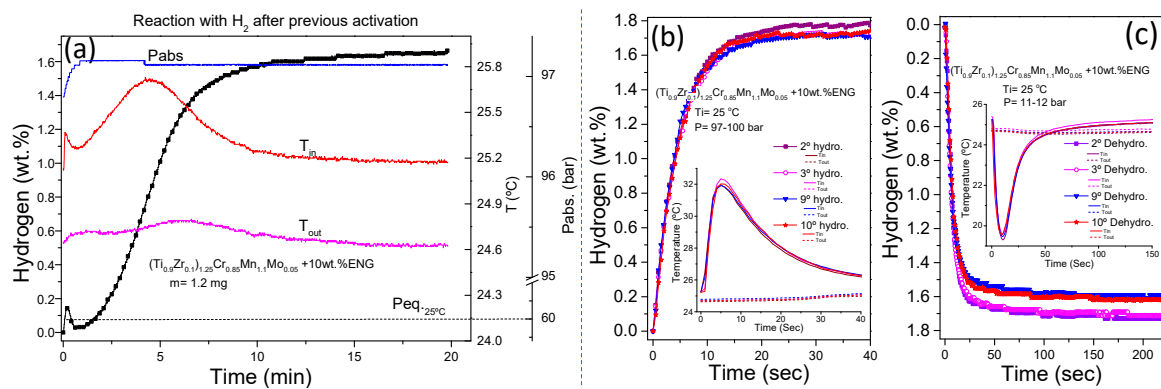

Figure 6. (**a**) First active hydrogenation of $(Ti_{0.9}Zr_{0.1})_{1.25}Cr_{0.85}Mn_{1.1}Mo_{0.05}$ + 10 wt.% ENG under around 100 bar and 25 °C, and (**b**) hydrogenation and (**c**) dehydrogenation cycling under 97–100 bar and 11–12 bar for $(Ti_{0.9}Zr_{0.1})_{1.25}Cr_{0.85}Mn_{1.1}Mo_{0.05}$ + 10 wt.% ENG (m = 1.2 g, Sieverts apparatus [62]).

After hydrogen cycling, the bulk density of the $(Ti_{0.9}Zr_{0.1})_{1.25}Cr_{0.85}Mn_{1.1}Mo_{0.05}$ + 10 wt.% ENG material was determined by the weight-volume method, measurements in a pycnometer, and compared with the tamped density. From the weight-volume method, a bulk density of 1.250 ± 0.015 g/cm^3 was registered. From the measurement in the gas pycnometer, the crystalline density of the material amounted to 5.4962 ± 0.0073 g/cm^3. In addition, the compacted density (after compression by several jolts) was 1.285 ± 0.010 g/cm^3. There is no marked difference between the measured bulk and tamped density. The porosity of the material, calculated by Equation (1) and considering the bulk and crystalline densities, is 0.77.
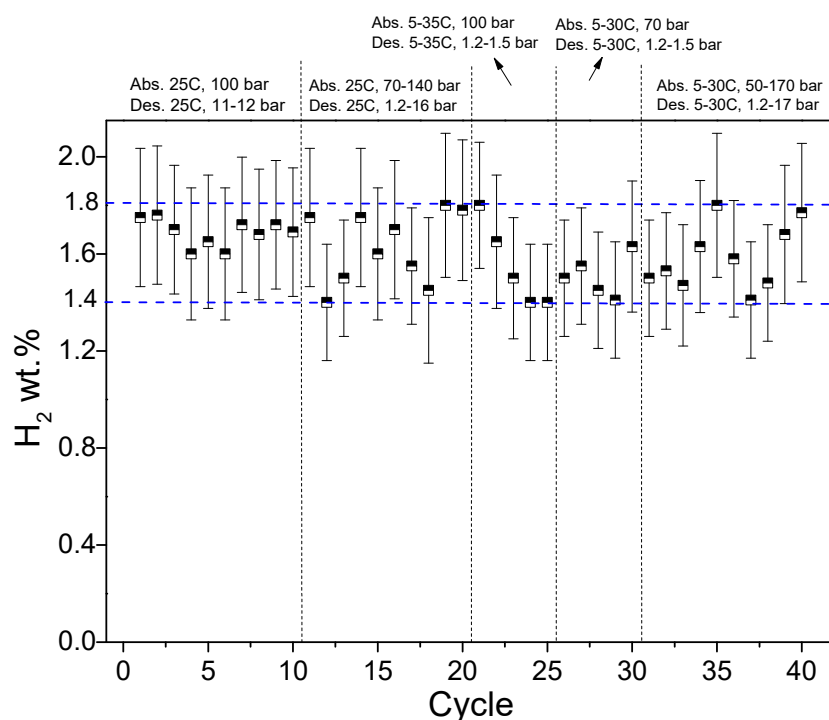
Figure 7. Hydrogen capacity upon cycling for $(Ti_{0.9}Zr_{0.1})_{1.25}Cr_{0.85}Mn_{1.1}Mo_{0.05}$ + 10 wt.% ENG after activation. Values of dehydrogenation capacity (m = 300 mg, Sieverts apparatus [62]).

4. Discussion

In this section, the parameters considered for the design of the alloy, the procedure to add ENG, and the beneficial effects of ENG on the hydrogen storage properties of the alloy are discussed. The potential application of the designed material in a hybrid tank is also analyzed based on a model that we modified to take into consideration practical concerns [53,66].

4.1. Design of the $(Ti_{0.9}Zr_{0.1})_{1.25}Cr_{0.85}Mn_{1.1}Mo_{0.05}$ added 10wt.% ENG Material

In this work, the material for the hybrid concept was developed based on three premises: (1) the already reported targets for the design of alloys to be used as a solid-state hydrogen storage material for the hybrid concept [25,28,56], (2) the substitutional effects of different elements on AB_2 alloys [15,19,22,24,25,28,30,31,34,41,42,45,48], and (3) practical design parameters [8,30,57,67,68].

Concerning the first premise, Mori et al. [56] proposed the synthesis of high-equilibrium pressure alloys for 350 bar vessels with capacities over 3.0 wt.% H_2, reaction enthalpy $\Delta H \leq 20$ kJ/mol H_2, $P_{eq.}$ for dehydrogenation ($P_{eq.des.}$) > 10 bar at −30 °C, $P_{eq.}$ for hydrogenation ($P_{eq.abs.}$) < 350 bar at 120 °C and cycling stability within 1000 cycles with less than 10 % of loss of hydrogen capacity. Then, it was suggested that high-pressure alloys should meet more practical characteristics for their application in a coupled hybrid tank-fuel cell system, such as $P_{eq.}$ for dehydrogenation ($P_{eq.des.}$) > 10 bar at 0 °C, $P_{eq.des.} \leq 120$ bar at 80 °C and $\Delta H \approx 20$ kJ/mol H_2 [25,28]. None of the synthesized materials for the hybrid tank application can meet all the set requirements, particularly the hydrogen capacity higher than 3.0 wt.% and both operative pressure constraints at the same time [11,14,19,24,25,28,34,36,48,50,52]. However, the proposed requirements are a guideline for the material's design.

Regarding the second premise, AB_2 C14 Laves alloys are among the best potential materials with relatively high desorption pressures, moderate hydrogen capacity, fast kinetic behavior, and relatively easy activation [15,19,22,25,30,31,34,41,42,45,48]. Non-stoichiometric Ti-Cr-based alloys with AB_2 C14 Laves structure offer more flexibility to tailor the hydrogen capacity and equilibrium pressures by the substitution of elements without losing the C14 Laves structure [15,19,22,25,34,41,42,45]. In this respect,

the equilibrium pressure of metal hydrides is proportional to the quotient of bulk modulus (B) and cell volume (Vo) ratio, ln $P \sim (B/Vo)$. Additionally, there is a dependence of the hydride capacity on the cell volume (Vo), i.e., higher Vo allows the allocation of more interstitial hydrogen, increasing the hydrogen capacity, but lowering the equilibrium pressure [48,69]. In general, high equilibrium pressures correspond to low reaction enthalpy, but lower hydrogen capacity [11,19,24,25,28,34,41,45,48,50,52].

In Section 3.1, the results of the designed non-stoichiometric Ti-Cr-based alloy were shown. It was already reported that the partial substitution of Mn for Cr causes a contraction of the unit cell that increases the H-lattice elastic interaction, leading to lower stabilities. Therefore, Ti-Cr-Mn presents reduced reaction enthalpy, allowing it to reach the target of 20 kJ/mol H_2 [70]. In the composition of our designed material, instead of having a Mn:Cr ratio equal to 1, a Mn:Cr ratio of about 1.3 was obtained, which provided enthalpies for hydrogenation and dehydrogenation near the target (Figure 2c). It is important to mention that the amount of Mn is difficult to set since its high vapor pressure results in its easy evaporation during the arc-melting process.

The substitution of Ti for Zr in the A sites enhances the hydrogen storage capacity, accelerates the hydrogenation kinetic behavior, and also, enhances the activation of the material [21,35,42]. However, Zr has a strong effect on decreasing the equilibrium pressure [71,72]. Zr has a larger atomic radius than Ti (Zr: 0.160 nm and Ti: 0.146 nm) and a smaller bulk modulus (Zr: 83.3 GPa and Ti: 105.1 GPa) [73]. Therefore, the effect of the atomic radius on the increase in the cell volume results in a decrease in the equilibrium pressure and more interstitial space to allocate hydrogen. The partial substitution of Ti for Zr in a $Ti_{1.1}CrMn$ led to an increase in the hydrogen capacity from 1.9 to 2.2 wt.% for $(Ti_{0.9}Zr_{0.1})_{1.1}CrMn$. This increase in capacity was associated with an enhancement of the hydrogenation kinetic behavior [42]. The increased substitution of Ti for Zr in $(Ti_{1-x}Zr_x)_{1.1}CrMn$ alloy increases the dehydrogenation enthalpy: 22.9 kJ/mol H_2 (x = 0), 25.5 kJ/mol H_2 (x = 0.1), 26.6 kJ/mol H_2 (x = 0.15) and 28.3 kJ/mol H_2 (x = 0.2) [25]. The increase in the Zr amount from x = 0 to x = 0.11 leads to a decrease in the equilibrium pressure of dehydrogenation at 0 °C from about 35 to 10 bar and a further increase results in lower dehydrogenation equilibrium pressure [25]. It was also reported that the presence of Zr as an added component in a Zr_7Ni_{10} alloy to Ti-V-Cr alloy improves the activation of the alloy, related to the presence of Zr and Ni-rich phase at the grain boundaries in a single melt alloy [21].

Kojima et al. [48] suggested that the Ti content should be between 1.0 and 1.16 (in atomic ratio). On the one hand, for a Ti content below 1.0, the alloy presents insufficient activation because of extremely high equilibrium pressure. On the other hand, for a Ti content above 1.16, the marked decreased in the dehydrogenation equilibrium pressure leads to irreversibly stored hydrogen. For the alloy herein designed, the Ti content is in the suggested range (Ti = 1.125) in order to have proper activation behavior and an equilibrium pressure in the desired range. The composition of the A sites elements, i.e., $(Ti_{1-x}Zr_x)_{1.125}$ with x = 0.1 did not provide a hydrogen capacity larger than 1.5 wt.%. Nevertheless, the hydrogen capacity is also determined by the presence of other elements in the alloy. The set amount of Zr in the A sites allowed keeping the dehydrogenation enthalpy at 24.1 kJ/mol H_2 (Figure 2c). The alloy was activated in the first hydrogenation process (Figure 3a), and this can be associated with the proper proportion of Ti and the presence of well-distributed Zr (Figure 4b), as well as the big particles of materials introduced in the reactor, since the surface exposed to the oxidation was not large.

In order to tune the equilibrium pressures, Cr was substituted by Mo in the B sites. The introduction of Mo results in the increase in cell volume owing to the large radii of Mo (Cr: 0.128 nm and Mo: 0.140 nm). Nevertheless, the bulk modulus of Mo is notably larger than the one of Cr (Cr: 190.1 GPa and Mo: 272.5 GPa). Hence, the effect of the larger bulk modulus of Mo is more pronounced than the increase in the cell volume, and for this reason, the equilibrium pressure increases with the amount of Mo [11,18,25,48]. Cao et al. [25] observed an almost linear increase in the dehydrogenation equilibrium pressure with the amount of Mo for $(Ti_{0.85}Zr_{0.15})_{1.1}Cr_{1-x}Mo_xMn$ alloy (x = 0 to 0.15). However, with an amount of Mo higher than x = 0.05, the hydrogen capacity drastically drops. Thus, the composition of the designed alloy in this work is 0.05; $(Ti_{0.9}Zr_{0.1})_{1.25}Cr_{0.85}Mn_{1.1}Mo_{0.05}$.

Some Fe as an impurity was detected. However, its effects were neglected because of the low weight %. Fe substitutes Cr in the B sites and results in a strong increase in the equilibrium pressure, but a decrease in the hydrogen capacity [19]. It is conceivable that the small amount of Fe might have had an effect on reducing the wt.% H_2.

As mentioned above, the equilibrium pressure is proportional to the ratio between the bulk modulus and the volume of the cell of the alloy (*B/Vo*). Comparing with the already published best AB_2 C14 alloys for the hybrid application, the compositions were determined to obtain a suggested dehydrogenation equilibrium pressure slightly over 10 bar at 0 °C. As seen in Figure 8, there is a general trend towards increasing the equilibrium pressure at the larger *B/Vo* ratio. For an alloy without the addition of pure Fe, we considered that a *B/Vo* ratio of about 7×10^{23} GPa/cm^3 would result in a dehydrogenation pressure at 0 °C slightly higher than 10 bar and moderate hydrogenation equilibrium pressures. In Appendix D, all the equations and data used for the calculations can be seen.

The third premise for the design is related to practical parameters. The addition of 10 wt.% ENG by a non-energetic mechanical method improved the kinetic behavior of the alloy, reducing the hydrogenation and dehydrogenation times (compare Figures 3 and 6) without changing either the crystal structure of the material (Figures 1 and 4), the thermodynamic behavior of the material (Figure 2) or the hydrogen capacity of about 1.5 wt.% (Figures 3, 6 and 7). ENG reduces the increase/decrease in temperature upon hydrogenation/dehydrogenation practically by half from about 11 to 5 °C (Figures 3 and 6), due to a more efficient heat transfer and consequently improving the kinetic behavior of the $(Ti_{0.9}Zr_{0.1})_{1.25}Cr_{0.85}Mn_{1.1}Mo_{0.05}$ + 10 wt.% ENG material. Moreover, the addition of ENG increases the porosity of the material from 0.54 to 0.77, since the bulk density diminishes. This fact is associated with the low weight of ENG and its larger particle size distribution between 50 and 200 μm (Figure 5). On the one hand, it allows a larger amount of hydrogen in the gas phase and acts as a buffer for the expansion of the alloy upon hydrogenation [64,65]. On the other hand, it diminishes the packing density of the metal hydride. This issue is further discussed in the next section.
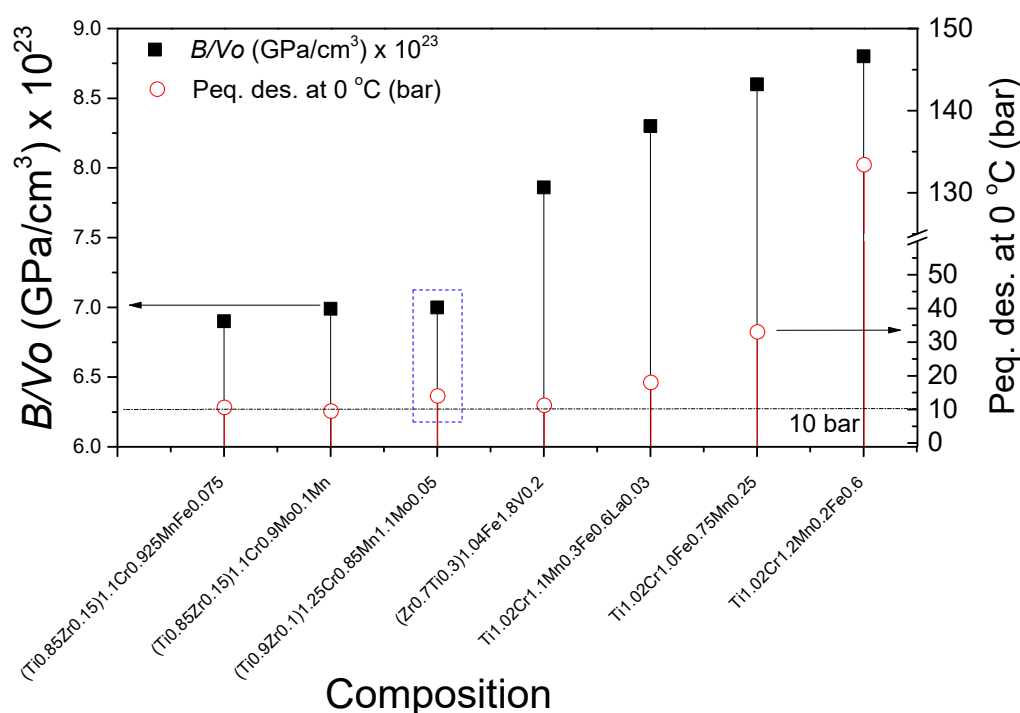

Figure 8. Ratio of bulk modulus and cell volume of the alloys and dehydrogenation equilibrium pressures at 0 °C for the best AB_2 C14 compositions for the hybrid concept and the herein obtained alloy [19,22,25,28,34,45].

Takeichi et al. [31] investigated the structural and hydrogen storage properties of Ti-Cr alloy by arc-melting and mechanical milling. After milling, the C14 Laves alloy obtained by arc-melting transformed to BCC structure. TEM observations showed an amorphous-like structure on the surface of the particles and the grain boundaries of the alloy after mechanical milling. The loss of hydrogen capacity of the material after the grinding process was ascribed to these amorphous-like structures, where hydrogen cannot be placed. Somo et al. reported in a review about mechanical milling applied to metal alloys that as-milled alloys are more prone to oxide layer formation, hindering the fast hydrogen absorption, and in several cases, diminishing the capacity [74]. Hence, a non-energetic mixing procedure was chosen as the most feasible method for laboratory and larger scales. It is true that the mixing process was carried out with the $(Ti_{0.9}Zr_{0.1})_{1.25}Cr_{0.85}Mn_{1.1}Mo_{0.05}$ alloy after cycling because of the reduced particle size. The obtained $(Ti_{0.9}Zr_{0.1})_{1.25}Cr_{0.85}Mn_{1.1}Mo_{0.05}$ + 10 wt.% ENG material was harder to activate because of the oxide layer that might have been formed during the mixing process. Even though a thermal process was required, the highest temperature used for the activation was 100 °C. This temperature is compatible with the maximum temperature of 120 °C that an aluminum liner and carbon-reinforced fiber tank can stand [75], so that an in-place activation is feasible.

According to the standard for safety, the high-pressure hydrogen tank cannot heat up more than 85 °C during refueling [67]. Hence, this temperature limit is related to absorption equilibrium pressure, which in our case is 248 ± 50 bar at 85 °C (Figure 2a). The range of temperature for practical application of AB_2 C14 Laves metal hydrides in hydrogen storage reservoirs coupled to a direct borohydride fuel cell (DBFC) or a low temperature proton exchange membrane fuel cell (LT-PEMFC) is between 20 and 85 °C, which offers a broader temperature range [8]. Another important practical parameter is the cost of the alloy. As described in Section 1, the designed AB_2 alloy does not contain highly expensive elements such as V. In fact, a metal alloy manufacturer provided a cost of 80 US$/kg for the herein designed alloy $((Ti_{0.9}Zr_{0.1})_{0.125}Cr_{0.85}Mn_{1.1}Mo_{0.05})$ [68], which represents a reasonable cost for its employment in a scaled-up hybrid tank.

Table 1 displays the main hydrogen storage properties for the best-selected alloys synthesized in previous publications [19,22,25,28,34,45,48] and the material produced in this work. As seen, the dehydrogenation enthalpy is near the set target of 20 kJ/mol H_2 and all the equilibrium pressures at 0 °C are over 10 bar. Some alloys also present an actual dehydrogenation equilibrium pressure over 10 bar at −30 °C, but the equilibrium pressures at higher temperatures become extremely large and might be a limitation for their employment. The hydrogen capacity ranges between 1.5 and 1.8, which in our case is in the error band of the Sieverts device. Considering that the capacities are relatively low and the kinetic behaviors are in general quite fast, the error at the time to measure the capacity is not to be neglected; no error band is reported for the compositions listed in Table 1 [19,22,25,28,34,45,48]. Hence, we consider that the design material has a suitable capacity. There is a lot of dispersion in terms of cycling stability and times for the hydrogenation and dehydrogenation. There are two works in which the cycling stability was measured after 200 and 1000 cycles, and proper material stability was obtained [28,48], but in most of the cases, the cycling stability is evaluated between 10 to 50 cycles and not all the cycling conditions are described [18,21,24,33,44]. In our case, we performed 10 cycles under homogeneous conditions for the alloy (Figure 3) and the material (alloy + ENG, Figure 6), and 40 cycles under variable conditions (Figure 7). The $(Ti_{0.9}Zr_{0.1})_{1.25}Cr_{0.85}Mn_{1.1}Mo_{0.05}$ + 10 wt.% ENG showed capacities within the error bars (Figure 7). Finally, the abs./des. times of our material shows quite fast kinetic behavior and this can be attributed to the alloy itself and the addition of ENG enhancing the effect heat of dissipation, even with a low amount of material, since a notable rise of temperature is observed (Figures 3 and 6).

Table 1. Comparison of the main hydrogen storage properties among materials developed for the hybrid concept.

Reference	Composition	$\Delta H_{des.}$ (kJ/mol H_2)	$P_{eq.des.}$ ($-30\,°C$) (bar) [1]	$P_{eq.des.}$ ($0\,°C$) (bar) [1]	wt.% H_2 [2]	Cycling Stability	Hydro./Dehydro. Times and Conditions
[48]	$Ti_{1.1}CrMn$	22	15.7	51.8	1.8	1000 cycles with 94 % of the initial capacity	Abs. under 330 bar and 23 °C in 60 s/Des. 1 bar and 23 °C in 300 s
[19]	$Ti_{1.02}Cr_{1.2}Mn_{0.2}Fe_{0.6}$	16.67	53.9	133.4	1.61	10 cycles at 218 bar and $-10\,°C$/No loss of capacity	Abs. under 218 bar and $-10\,°C$ in 900 s
[21]	$(Ti_{0.85}Zr_{0.15})_{1.1}Cr_{0.925}MnFe_{0.075}$	25.4	2.7	10.6	1.54	50 cycles with no hydrogen lost (shown Des. 0 °C)	Des. 1 bar and at 0 °C in 360 s/Des. 1 bar and at 30 °C in 120 s (Abs. N.A.)
[25]	$(Ti_{0.85}Zr_{0.15})_{1.1}Cr_{0.9}Mo_{0.1}Mn$	23.7	2.7	9.5	1.78	50 cycles with no hydrogen lost (shown Des. 0 °C)	Des. 1 bar and at 0 °C in 420 s/Des. 1 bar and at 25 °C in 120 s (Abs. N.A.)
[28]	$(Zr_{0.7}Ti_{0.3})_{1.04}Fe_{1.8}V_{0.2}$	23.5	3.12	11.2	1.51	200 cycles with stable capacity	Des. 1 bar and at 0 °C in 480 s/Des. 1 bar and at 25 °C in 300 s (Abs. N.A.)
[34]	$Ti_{1.02}Cr_{1.1}Mn_{0.3}Fe_{0.6}La_{0.03}$	16.63	7.4	18	1.715	N.A.	N.A.
[45]	$Ti_{1.02}Cr_{1.0}Fe_{0.75}Mn_{0.25}$	19	12	33	1.85	N.A.	Des. at $-40\,°C$ in 180 s (Abs. N.A.)
This work	$(Ti_{0.9}Zr_{0.1})_{1.25}Cr_{0.85}Mn_{1.1}Mo_{0.05}$ + 10 wt.% ENG[3]	24	4	14	1.5	40 cycles with stable capacity (within the error bar)	Abs. 97–100 bar and about 25 °C in 25 s/Des. 11–12 bar about 25 °C in 70 s

[1] Calculated from the reported dehydrogenation enthalpy, entropy, and equilibrium pressures. [2] Maximum capacity. [3] Capacity, cycling stability, and abs./des. times from the alloy + 10ENG. N.A.: Not available, Abs.: Absorption and Des.: Desorption.

4.2. Potential Application of $(Ti_{0.9}Zr_{0.1})_{0.125}Cr_{0.85}Mn_{1.1}Mo_{0.05}$ added 10 wt.% ENG Material in a Hybrid Tank

Takeichi et al. [53] evaluated the weight and volume of a hybrid tank based on a reinforced tank for 350 bar of 18 kg of weight and the ratio of the aluminum liner to the CFRP (Carbon Fiber Reinforced Polymer) layer of 1:1. For the calculation, it was assumed an alloy with 5 g/cm^3 of crystalline density with 3.0 wt.% H_2 capacity, an expansion of the alloy's volume of 20 % upon hydrogenation and a degree of filling of the alloy in the tank up to 40 %. For the calculation of the gas molar volume, the compressibility factor was considered to account for real gas behavior. They claimed that the tank could reach a little less than 4.1 wt.% H_2, and the volumetric density is notably improved by about 50 %. Cao et al. [22,25,28] evaluated the volumetric and gravimetric hydrogen density with equations reported by Ge et al. [66] for a 350 bar high-pressure tank with 100 L of inner volume and 11 kg of weight. They took into account the van der Waals equation for the determination of the gas molar volume. For the calculations of the hydrogen amount in the alloy, the crystalline density of the alloys with a degree of filling in the tank up to 50 % of the volume was considered (assuming 0.5 for the material's porosity). The evaluation was done at 25 °C, and 350 bar for the developed materials, aiming to determine the degree of filling of the alloy in the tank, mainly in order to fulfill the 40 kg H_2/m^3 system and to verify the 0.055 kg H_2/kg system (5.5 wt.% H_2) set by the DOE 2017–2020 [76]. All the assessed materials reached the hydrogen volumetric density target with a degree of filling lower than 50 % of the volume, but failed to meet the hydrogen gravimetric density: $(Ti_{0.85}Zr_{0.15})_{1.1}Cr_{0.925}MnFe_{0.075}$: 41 % of filling and 1.49 wt.% [22], $(Ti_{0.85}Zr_{0.15})_{1.1}Cr_{0.9}Mo_{0.1}Mn$: 28% of filling and 2.72 wt.% [25], and $(Zr_{0.7}Ti_{0.3})_{1.04}Fe_{1.8}V_{0.2}$: ~30 % and 1.95 wt.% (under 25 °C and 120 bar: 48 % and 1.45 wt.%) [28]. In these works [22,25,28,53], the additional weight and reduction in internal volume or increase in the external volume because of a cooling/heating system was not contemplated. By applying the model of Ge et al. [66] for the $(Ti_{0.9}Zr_{0.1})_{1.25}Cr_{0.85}Mn_{1.1}Mo_{0.05}$ + 10 wt.% ENG in a hybrid tank of 100 L and 11 kg, 40 kg H_2/m^3 system is reached with a degree of filling of 41 %, with about 2 wt.% of hydrogen capacity (equations and table of the calculations are in Appendix E).

For the calculations of the hydrogen density in the hybrid tank, the experimentally determined properties of the hydrogen-absorbing material, $(Ti_{0.9}Zr_{0.1})_{1.25}Cr_{0.85}Mn_{1.1}Mo_{0.05}$ + 10 wt.% ENG,

are included: the porosity of the material ($\varepsilon = 0.77$), the determined crystalline density (5.4962 ± 0.0073 g/cm^3) and the hydrogen capacity (1.5 wt.%). We also assume an expansion of the alloy's volume upon hydrogenation of 25 %, which causes an additional reduction in the gas phase volume [77]. It was suggested that the maximum degree of filling of the alloy in the tank for safe mechanical stability, owing to stress created by the swelling of the hydride should be 61 %, considering the bulk density of the material [78,79]. This value is consistent with the porosity of the material, determined after cycling (final size and shape of the alloy's particles) and the assumed volumetric expansion upon hydrogenation. For the high-pressure gas phase, a real gas state equation correlated with the NIST database is used [80,81]. We also contemplate that the tank always includes an internal cooling/heating system, given the features of a reinforced tank, which reduces in 20 % its internal volume and increases its weight by 15 %. For the vessel, an Al-liner and CRFP tank with a cylindrical body and hemispherical caps and with a liner to CRFP weight ratio of 1, as proposed in Reference [53], are assumed. All the details and equations are in Appendix E. As seen in Figure 9, the hydrogen gravimetric and volumetric capacity for the proposed Al-liner and CRFP shell of 34 L of internal volume filled with the $(Ti_{0.9}Zr_{0.1})_{1.25}Cr_{0.85}Mn_{1.1}Mo_{0.05}$ + 10 wt.% ENG are far from the DOE targets.
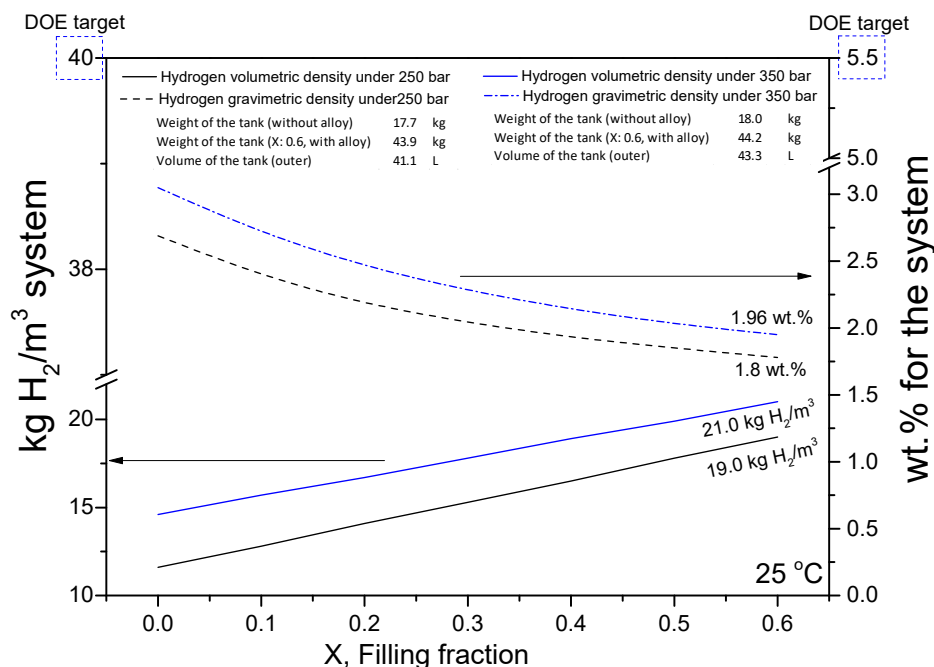

Figure 9. Curves of the hydrogen volumetric and gravimetric capacity of the hybrid tank as a function of the degree of filling of the alloy.

The gain of hydrogen volumetric density by the addition of the alloy is considerable and in the range of 40 % to 60 %, but with a penalty in the gravimetric capacity. It would be possible to combine several storage units in order to increase both hydrogen densities. Moreover, it is possible to observe that a reduction in pressure up to 250 bar does not cost a considerable loss of capacity and represents a strategy to be considered. It is particularly important in this case since it allows working below the maximum temperature of 85 °C for refueling [67], given the absorption equilibrium pressure of our material, i.e., 248 ± 50 bar at 85 °C (Figure 2a).

5. Conclusions

In this work, a strategy was developed to design a material for its application in a hybrid reservoir. A $(Ti_{0.9}Zr_{0.1})_{1.25}Cr_{0.85}Mn_{1.1}Mo_{0.05}$ + 10 wt.% ENG material composed of a non-stoichiometric AB_2 C14 Laves alloy and ENG with suitable hydrogen storage properties for the hybrid concept

was designed. This material has proper thermodynamic stability (nearby 20 kJ/mol H_2), adequate equilibrium pressures to work in the range between 0 °C ($P_{eq.des.}$ = 14 bar), and 85 °C ($P_{eq.abs.}$ = 248 bar), 1.5 wt.% of hydrogen capacity as well as abs./des. times of 25 and 70 s, respectively. Furthermore, the designed material showed enhanced thermal properties for a reduced high-pressure application at 250 bar coupled with a fuel cell. The evaluation of the applicability of the designed material into a reinforced high-pressure tank of 34 L of internal volume was done with a modified model. Applying this model, the dependence of the hydrogen density on practical parameters such as the real porosity of the material, the volumetric expansion of the hydride, the degree of filling based on the swelling of the hydride and the weight and volume of an internal cooling heating system, was considered. The proposed hybrid system under reduced pressure of 250 bar and with a filling degree material of 60% presented a hydrogen volumetric and gravimetric density of 19 kg H_2/m^3 system and 1.8 wt.%, respectively. Despite the fact that these values are far away from the DOE settings, it represents a strategy to think about a novel system configuration heading towards lower pressures and taking advantage of the additional hydrogen volumetric density of metal hydrides. More work is still ongoing to model and prove the validity of different hybrid system configurations.

Conflicts of Interest: The authors declare no conflict of interest.

Appendix A

The following Figure shows an exemplary analysis for the blank measurement substraction performed to the kinetic curves. As seen, the effect of the drop of pressure upon the hydrogen capacity and internal temperature during the initial stage of the measurement did not change the hydrogen capacity (difference within the error band) and the temperature (small difference) substantially.

Appendix B

The table for the determination of the nominal composition and molecular weight of the herein synthesize alloy is shown.

Appendix C

In Table A2, the conditions for the cycling of the material shown in Figure 7 are described.

Table A1. Nominal composition of the and weight of the non-stoichiometric AB$_2$ alloy.

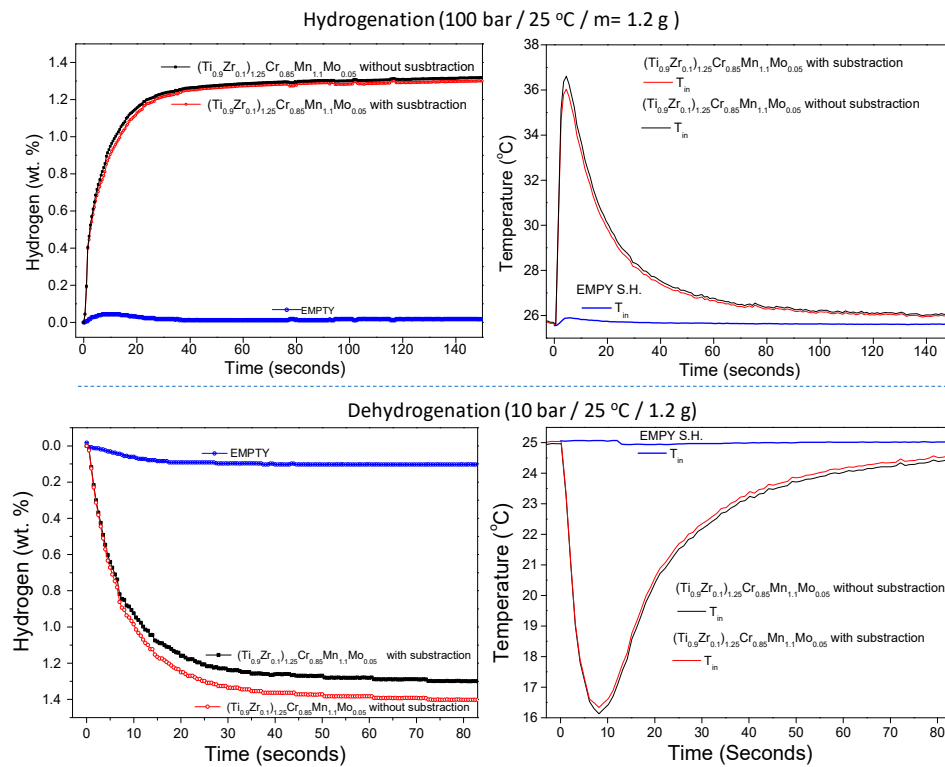| Elements	Atomic Fraction (EDX)	A	B/A	A	Elements	Amount	Elements' Atomic Weight (g)	Amount x Element Weight	Composition of the Alloy
Ti	0.337	0.375		1.25	Ti	1.250	47.86	53.8	(Ti0.9Zr0.1)1.25Cr0.85Mn1.1Mo0.05
Zr	0.038				Zr	0.125	91.224	11.6	
Cr	0.26	B	1.6	B	Cr	0.850	51.996	44.0	Weigh of the alloy (g/mol)
Mn	0.342	0.615		2	Mn	1.100	54.938	61.1	174.6
Mo	0.013				Mo	0.050	95.95	4.1	

Figure A1. Hydrogenation and dehydrogenation and their temperature profiles curves before and after blank subtraction.

Table A2. Cycling conditions for Figure 7.

N° of Cycle	Cycle Conditions	N° of Cycle	Cycle Conditions
1	Abs. 25C, 100 bar/Des. 25C, 11–12 bar	21	Abs. 9C, 100 bar/Des. 9C, 1.2–1.5 bar
2	Abs. 25C, 100 bar/Des. 25C, 11–12 bar	22	Abs. 5C, 100 bar/Des. 5C, 1.2–1.5 bar
3	Abs. 25C, 100 bar/Des. 25C, 11–12 bar	23	Abs. 10C, 100 bar/Des. 10C, 1.2–1.5 bar
4	Abs. 25C, 100 bar/Des. 25C, 11–12 bar	24	Abs. 35C, 100 bar/Des. 35C, 1.2–1.5 bar
5	Abs. 25C, 100 bar/Des. 25C, 11–12 bar	25	Abs. 35C, 100 bar/Des. 35C, 1.2–1.5 bar
6	Abs. 25C, 100 bar/Des. 25C, 11–12 bar	26	Abs. 30C, 70 bar/Des. 30C, 1.2–1.5 bar
7	Abs. 25C, 100 bar/Des. 25C, 11–12 bar	27	Abs. 25C, 70 bar/Des. 25C, 1.2–1.5 bar
8	Abs. 25C, 100 bar/Des. 25C, 11–12 bar	28	Abs. 20C, 70 bar/Des. 20C, 1.2–1.5 bar
9	Abs. 25C, 100 bar/Des. 25C, 11–12 bar	29	Abs. 15C, 70 bar/Des. 15C, 1.2–1.5 bar
10	Abs. 25C, 100 bar/Des. 25C, 11–12 bar	30	Abs. 5C, 70 bar/Des. 5C, 1.2–1.5 bar
11	Abs. 25C, 90 bar/Des. 25C, 1.8–2 bar	31	Abs. 5C, 50 bar/Des. 5C, 1.2–1.5 bar
12	Abs. 25C, 70 bar/Des. 25C, 3.5–4 bar	32	Abs. 5C, 50 bar/Des. 5C, 1.2–1.5 bar
13	Abs. 25C, 80 bar/Des. 25C, 2.5–2.7 bar	33	Abs. 10C, 50 bar/Des. 10C, 1.2–1.5 bar
14	Abs. 25C, 120 bar/Des. 25C, 3–3.5 bar	34	Abs. 10C, 90 bar/Des. 10C, 1.2–1.5 bar
15	Abs. 25C, 140 bar/Des. 25C, 7.53–8 bar	35	Abs. 5C, 75 bar/Des. 5C, 1.2–1.5 bar
16	Abs. 25C, 100 bar/Des. 25C, 15.5–16 bar	36	Abs. 15C, 100 bar/Des. 15C, 1.2–1.5 bar
17	Abs. 25C, 100 bar/Des. 25C, 15.5–16 bar	37	Abs. 20C, 130 bar/Des. 20C, 3.3–3.5 bar
18	Abs. 25C, 100 bar/Des. 25C, 25.5–26 bar	38	Abs. 25C, 147 bar/Des. 20C, 2.0–2.1 bar
19	Abs. 25C, 100 bar/Des. 25C, 1.2–1.5 bar	39	Abs. 30C, 160 bar/Des. 30C, 2.0–2.2 bar
20	Abs. 25C, 100 bar/Des. 25C, 1.2–1.5 bar	40	Abs. 30C, 170 bar/Des. 30C, 16–17 bar

Appendix D

Calculations of the *B/Vo* ratio based on the equations reported by Kojima et al. [48]. All data were obtained from the book Kittel [73] and a materials database [80]. The compositions in atomic fraction and cell volumes were obtained from the respective publications listed in the table below.

Table A3. Properties of the elements for the calculation of the bulk modulus of alloys.

Density [71]	Value	Molecular Weight [71]	Value	Bulk Modulus [69]	Value
ρ Ti (g/cm^3)	4.58	M Ti (g/mol)	47.86	*B* Ti (GPa)	105.1
ρ Zr (g/cm^3)	6.45	M Zr (g/mol)	91.224	*B* Zr (GPa)	83.3
ρ Cr (g/cm^3)	7.25	M Cr (g/mol)	51.996	*B* Cr (GPa)	190.1
ρ Mn (g/cm^3)	7.65	M Mn (g/mol)	54.938	*B* Mn (GPa)	59.6
ρ Mo (g/cm^3)	10.02	M Mo (g/mol)	95.95	*B* Mo (GPa)	272.5
ρ Fe (g/cm^3)	7.874	M Fe (g/mol)	55.845	*B* Fe (GPa)	168.3
ρ V (g/cm^3)	6.11	M V (g/mol)	50.942	*B* V (GPa)	161.9
ρ La (g/cm^3)	6.162	M La (g/mol)	138.91	*B* V La (GPa)	24.3

$$x_i = \text{Atomic frction of the element } i$$

$$M_i = \text{Atomic weight of the element } i$$

$$\rho_i = \text{Density of the element } i$$

$$B_i = \text{Bulk modulus of the alloy}$$

$$V = \text{volume of the alloy}$$

$$B = \text{Bulk modulus of the alloy.}$$

$$V = \sum_{i=1}^{n} \frac{x_i M_i}{\rho_i} \tag{A1}$$

$$B = \sum_{i=1}^{n} \frac{B_i(x_i M_i / \rho_i)}{V} \tag{A2}$$

Table A4. Compositions, cell volume, bulk modulus and ratio between the bulk modulus and cell volume for AB2 C14 Lave alloys.

Reference	Composition	Atomic Fraction					Vo (cm^3)	B (GPa)	B/Vo (GPa/cm^3)
		Ti	Cr	Mn	-	-			
[12]	Ti$_{1.1}$CrMn	0.355	0.323	0.323	-	-	1.64×10^{-22}	116.0	7.079×10^{23}
[18]	Ti$_{1.02}$Cr$_{1.2}$Mn$_{0.2}$Fe$_{0.6}$	Ti	Cr	Mn	Fe	-	1.625×10^{-22}	142.6	8.775×10^{23}
		0.338	0.397	0.066	0.199	-			
[21]	(Ti$_{0.85}$Zr$_{0.15}$)$_{1.1}$Cr$_{0.925}$MnFe$_{0.075}$	Ti	Zr	Cr	Mn	Fe	1.656×10^{-22}	114.1	6.89×10^{23}
		0.274	0.048	0.298	0.322	0.024			
[24]	(Ti$_{0.85}$Zr$_{0.15}$)$_{1.1}$Cr$_{0.9}$Mo$_{0.1}$Mn	Ti	Zr	Cr	Mn	Mo	1.68×10^{-22}	117.4	6.998×10^{23}
		0.301	0.053	0.29	0.322	0.032			
[27]	(Zr$_{0.7}$Ti$_{0.3}$)$_{1.04}$Fe$_{1.8}$V$_{0.2}$	Ti	Zr	Fe	V	-	1.723×10^{-22}	135.5	7.864×10^{23}
		0.239	0.103	0.592	0.066	-			
[33]	Ti$_{1.02}$Cr$_{1.1}$Mn$_{0.3}$Fe$_{0.6}$La$_{0.03}$	Ti	Cr	Fe	Mn	La	1.6328×10^{-22}	135.8	8.317×10^{23}
		0.334	0.361	0.197	0.098	0.01			
[44]	Ti$_{1.02}$Cr$_{1.0}$Fe$_{0.75}$Mn$_{0.25}$	Ti	Cr	Fe	Mn	-	1.6126×10^{-22}	139.0	8.62×10^{23}
		0.343	0.32	0.253	0.084	-			
This work	(Ti$_{0.9}$Zr$_{0.1}$)$_{1.25}$Cr$_{0.85}$Mn$_{1.1}$Mo$_{0.05}$	Ti	Zr	Cr	Mn	Mo	1.656×10^{-22}	116.6	7.041×10^{23}
		0.337	0.38	0.26	0.342	0.013			

Appendix E

It was applied the model of Ge et al. [66] for a 350 bar high-pressure tank with Vinner = 100 L of inner volume, Vinner/Vouter = 1.2 and Wo = 11 kg of weight to the designed alloy. The equations and the results (Table A3) are as follows:

$$\rho_{H2\ gas} = \frac{P}{R_g(T + \alpha P)}\left(\frac{kg}{m^3}\right); \tag{A3}$$

Hydrogen density in the gas phase [81,82]

$$P = \text{pressure (Pa)}$$

$$T = \text{temperature (K)}$$

$$R_g = 4124.3\left(\frac{J}{kgK}\right)$$

$$\alpha = 1.9155 \times 10^{-6}\left(\frac{K}{Pa}\right)$$

$$Hv = \rho_{H2\ gas}V_{inner}(1 - x)\ (kg),\ \text{stored hydrogen in the gas phase} \tag{A4}$$

$$x = \text{degree of filling of the hydride in the tank}$$

$$Hm = \rho_{crist.\ alloy}\left(\frac{wt.\%}{100}\right)V_{inner}x\ (kg),\ \text{stored hydrogen in the solid phase(MH)} \tag{A5}$$

$$\rho_v = \frac{Hv + Hm}{V_{outer}}\left(\frac{kg\ H_2}{m^3\ system}\right),\ \text{hydrogen volumetric density} \tag{A6}$$

$$\rho_m = \frac{Hv + Hm}{\rho_{crist.\ alloy}V_{inner}x + W_o}\left(\frac{kg\ H_2}{kg\ system}\right),\ \text{hydrogen gravimetric density} \tag{A7}$$

$$t\ (\text{thickness}) = 3.25 + 11\left(\frac{P}{35}\right)(mm) \tag{A8}$$

Applying the modified model [53,66]:
The following sketch shows the geometry of the Al-liner + CRFP and the dimensions [53].

Table A5. Hydrogen volumetric and gravimetric density calculated with the model of Ge et al. 1.5 wt.%, Rho: 5496.2 kg/m^3, Vinner tank: 100 L, Vinner tank: 100 L, Weight of the tank: 11 kg.

	298 K, 350 bar	
X (Filling Fraction)	kg H$_2$/m^3 System	wt.%
0	19.4	21.1
0.1	24.3	4.4
0.2	29.2	2.90
0.3	34.2	2.33
0.4	39.1	2.03
0.5	44.0	1.85
0.6	49.0	1.72
0.7	53.9	1.63
0.8	58.8	1.57
0.9	63.8	1.51
1	68.7	1.47
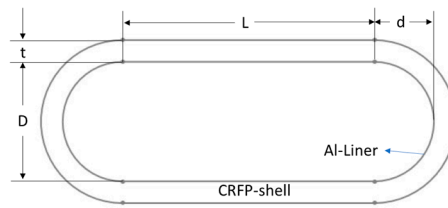
D	251.5 mm	Internal diameter of the vessel
L	580 mm	Length of the cylindrical part of the vessel
d	78.4 mm	Depth of the hemispheres at the ends of the vessel
L + 2d	736.8	Inner length of the vessel

Figure A2. Sketch of the Al-liner + CRFP and the dimensions.

Equations for the thickness, volume and weight of the tank:

$$t \text{ (thickness)} = 3.25 + 11\left(\frac{P}{35}\right)(\text{mm}) \tag{A9}$$

$$W_{tank} = 9 + 9\left(\frac{P}{35}\right)(\text{kg}) \tag{A10}$$

$$W_{\text{tank+cooling system}} = 1.15\, W_{tank}\ (\text{kg}); \ 15\% \text{ of additional weight} \tag{A11}$$

$$V_{\text{outer volume of the tank}} = \frac{\pi\left(\frac{D+2t}{2}\right)^2 L + \frac{4}{3}\pi(d+t)\left(\frac{D+2t}{2}\right)^2}{1 \times 10^6} \ (\text{L}); \ \text{external volume of the tank} \tag{A12}$$

$$V_{\text{inner volume of the tank}} = \frac{\pi\left(\frac{D}{2}\right)^2 L + \frac{4}{3}\pi d\left(\frac{D}{2}\right)^2}{1 \times 10^6} \ (\text{L}); \ \text{internal volume of the tank} \tag{A13}$$

$$V_{\text{inner volume of the tank}-\text{vol.cooling system}} = 0.8\, V_{\text{inner volume of the tank}} \ (\text{L}); 20\% \text{ of vol reduction} \tag{A14}$$

$$V_{\text{MH(without expansion)}} = V_{\text{inner volume of the tank}-\text{vol.cooling system}}[(1-\varepsilon)\, X] \ (\text{L}); \text{volume of the metal hyd.} \tag{A15}$$

$$V_{\text{MH}} = V_{\text{MH(without expansion)}} + \left(\beta\, V_{\text{MH(without expansion)}}\right)(\text{L}); \text{volume of alloy in hydrogenated state} \tag{A16}$$

ε = porosity of the hydride
β = Factor for the volumetric expansion of the alloy upon hydrogenation (0.25)
X = filling fraction of the alloy in the tank

$$V_{\text{gas phase}} = V_{\text{inner volume of the tank}-\text{vol.cooling system}} - V_{\text{MH}} \ (\text{L}); \text{volume of hydrogen gas} \tag{A17}$$

$$\rho_{\text{H2 gas}} = \frac{P}{R_g(T+\alpha P)}\left(\frac{\text{kg}}{\text{m}^3}\right); \tag{A18}$$

Hydrogen density in the gas phase [81,82]

$$P = \text{pressure (Pa)}$$

$$T = \text{temperature (K)}$$

$$Rg = 4124.3\left(\frac{\text{J}}{\text{kgK}}\right)$$

$$\alpha = 1.9155 \times 10^{-6}\left(\frac{\text{K}}{\text{Pa}}\right)$$

$$Hv = \rho_{\text{H2 gas}} V_{\text{gas phase}} \ (\text{g}), \ \text{stored hydrogen in the gas phase} \tag{A19}$$

$$Hm = \rho_{\text{alloy}}\left(\frac{\text{wt.\%}}{100}\right)V_{\text{MH}}(g), \text{ stored hydrogen in the solid phase(MH)} \tag{A20}$$

$$W_{MH} = H_m + \rho_{alloy}V_{MH} \text{ (g), weight of the alloy} \tag{A21}$$

$$\rho_v = \frac{Hv + Hm}{V_{\text{outer volume of the tank}}}\left(\frac{\text{kg H}_2}{\text{m}^3 \text{ system}}\right), \text{ hydrogen volumetric density} \tag{A22}$$

$$\rho_m = \frac{Hv + Hm}{W_{\text{tank+cooling system}} + W_{MH}}\left(\frac{\text{kg H}_2}{\text{kg system}}\right), \text{ hydrogen gravimetric density} \tag{A23}$$

Table A6. Hydrogen volumetric and gravimetric density calculated with the modified model.

25 °C, 250 bar			25 °C, 350 bar		
x (Filling Fraction)	Kg H$_2$/m^3 System	wt.%	x (Filling Fraction)	Kg H$_2$/m^3 System	wt.%
0	11.6	2.69	0	14.6	3.05
0.1	12.8	2.39	0.1	15.7	2.71
0.2	14.1	2.18	0.2	16.7	2.46
0.3	15.3	2.04	0.3	17.8	2.28
0.4	16.5	1.93	0.4	18.9	2.14
0.5	17.8	1.85	0.5	19.9	2.03
0.6	19.0	1.78	0.6	21.0	1.95

References

1. Chen, B.; Dong, L.; Liu, X.; Shi, G.Y.; Chen, L.; Nakajima, T.; Habib, A. Exploring the possible effect of anthropogenic heat release due to global energy consumption upon global climate: A climate model study. *Int. J. Climatol.* **2016**, *36*, 4790–4796. [CrossRef]
2. REN21. *Renewables 2019 Global Status Report*; REN21 Secretariat: Paris, France, 2019; ISBN 978-3-9818911-7-1. Available online: http://www.ren21.net/gsr-2019/ (accessed on 26 July 2019).
3. OECD/IEA. Global Energy and CO2 Status Report. Available online: https://www.iea.org/geco/ (accessed on 25 May 2019).
4. Le Quéré, C.; Andrew, R.M.; Friedlingstein, P.; Sitch, S.; Pongratz, J.; Manning, A.C.; Korsbakken, J.I.; Peters, G.P.; Canadell, J.G.; Jackson, R.B.; et al. Global Carbon Budget 2018 (pre-print). *Earth Syst. Sci. Data Discuss.* **2018**, 1–54. [CrossRef]
5. Heuser, P.; Grube, T.; Heinrichs, H.; Robinius, M.; Stolten, D. Worldwide Hydrogen Provision Scheme Based on Renewable Energy. 2020, pp. 1–27. Available online: https://www.preprints.org/manuscript/202002.0100/v1 (accessed on 25 April 2020).
6. Hobein, B.; Krüger, R. *Hydrogen and Fuel Cells*; Stolten, D., Ed.; WILEY–VCH: Weinheim, Germany, 2010; pp. 377–393.
7. Andersson, J.; Grönkvist, S. Large-scale storage of hydrogen. *Int. J. Hydrogen Energy* **2019**, *44*, 11901–11919. [CrossRef]
8. Lototskyy, M.V.; Tolj, I.; Pickering, L.; Sita, C.; Barbir, F.; Yartys, V. The use of metal hydrides in fuel cell applications. *Prog. Nat. Sci. Mater. Int.* **2017**, *27*, 3–20. [CrossRef]
9. Lai, Q.; Sun, Y.; Wang, T.; Modi, P.; Cazorla, C.; Demirci, U.B.; Ares Fernandez, J.R.; Leardini, F.; Aguey-Zinsou, K.F. How to Design Hydrogen Storage Materials? Fundamentals, Synthesis, and Storage Tanks. *Adv. Sustain. Syst.* **2019**, *3*, 1–64. [CrossRef]
10. Bellosta von Colbe, J.; Ares, J.R.; Barale, J.; Baricco, M.; Buckley, C.; Capurso, G.; Gallandat, N.; Grant, D.M.; Guzik, M.N.; Jacob, I.; et al. Application of hydrides in hydrogen storage and compression: Achievements, outlook and perspectives. *Int. J. Hydrogen Energy* **2019**, *44*, 7780–7808. [CrossRef]
11. Matsunaga, T.; Kon, M.; Washio, K.; Shinozawa, T.; Ishikiriyama, M. TiCrVMo alloys with high dissociation pressure for high-pressure MH tank. *Int. J. Hydrogen Energy* **2009**, *34*, 1458–1462. [CrossRef]
12. Sivov, R.B.; Zotov, T.A.; Verbetsky, V.N. Hydrogen sorption properties of ZrFex (1.9 ≤ x ≤ 2.5) alloys. *Int. J. Hydrogen Energy* **2011**, *36*, 1355–1358. [CrossRef]

13. Zotov, T.A.; Sivov, R.B.; Movlaev, E.A.; Mitrokhin, S.V.; Verbetsky, V.N. IMC hydrides with high hydrogen dissociation pressure. *J. Alloys Compd.* **2011**, *509*, S839–S843. [CrossRef]

14. Tsukahara, M. Hydrogenation properties of vanadium-based alloys with large hydrogen storage capacity. *Mater. Trans.* **2011**, *52*, 68–72. [CrossRef]

15. Young, K.; Nei, J.; Huang, B.; Fetcenko, M.A. Studies of off-stoichiometric AB2 metal hydride alloy: Part 2. Hydrogen storage and electrochemical properties. *Int. J. Hydrogen Energy* **2011**, *36*, 11146–11154. [CrossRef]

16. Aoki, M.; Noritake, T.; Ito, A.; Ishikiriyama, M.; Towata, S.I. Improvement of cyclic durability of Ti-Cr-V alloy by Fe substitution. *Int. J. Hydrogen Energy* **2011**, *36*, 12329–12332. [CrossRef]

17. Mitrokhin, S.; Zotov, T.; Movlaev, E.; Verbetsky, V. Hydrogen interaction with intermetallic compounds and alloys at high pressure. *J. Alloys Compd.* **2013**, *580*, S90–S93. [CrossRef]

18. Verbetsky, V.N.; Zotov, T.A.; Movlaev, E.A. Absorption of hydrogen by V-Mo and V-Mo-Ti alloys. *Inorg. Mater. Appl. Res.* **2014**, *5*, 70–74. [CrossRef]

19. Chen, Z.; Xiao, X.; Chen, L.; Fan, X.; Liu, L.; Li, S.; Ge, H.; Wang, Q. Influence of Ti super-stoichiometry on the hydrogen storage properties of Ti1+xCr1.2Mn0.2Fe0.6 (x = 0–0.1) alloys for hybrid hydrogen storage application. *J. Alloys Compd.* **2014**, *585*, 307–311. [CrossRef]

20. Lototskyy, M.V.; Yartys, V.A.; Pollet, B.G.; Bowman, R.C. Metal hydride hydrogen compressors: A review. *Int. J. Hydrogen Energy* **2014**, *39*, 5818–5851. [CrossRef]

21. Bibienne, T.; Bobet, J.L.; Huot, J. Crystal structure and hydrogen storage properties of body centered cubic 52Ti-12V-36Cr alloy doped with Zr7Ni10. *J. Alloys Compd.* **2014**, *607*, 251–257. [CrossRef]

22. Cao, Z.; Ouyang, L.; Wang, H.; Liu, J.; Sun, L.; Zhu, M. Composition design of Ti-Cr-Mn-Fe alloys for hybrid high-pressure metal hydride tanks. *J. Alloys Compd.* **2015**, *639*, 452–457. [CrossRef]

23. Shen, C.C.; Li, H.C. Cyclic hydrogenation stability of γ-hydrides for Ti25V35Cr40 alloys doped with carbon. *J. Alloys Compd.* **2015**, *648*, 534–539. [CrossRef]

24. Jiang, L.; Tu, Y.; Tu, H.; Chen, L. Microstructures and hydrogen storage properties of ZrFe2.05−xVx (x = 0.05–0.20) alloys with high dissociation pressures for hybrid hydrogen storage vessel application. *J. Alloys Compd.* **2015**, *627*, 161–165. [CrossRef]

25. Cao, Z.; Ouyang, L.; Wang, H.; Liu, J.; Sun, D.; Zhang, Q.; Zhu, M. Advanced high-pressure metal hydride fabricated via Ti-Cr-Mn alloys for hybrid tank. *Int. J. Hydrogen Energy* **2015**, *40*, 2717–2728. [CrossRef]

26. Jain, P.; Dixit, V.; Jain, A.; Srivastava, O.N.; Huot, J. Effect of magnesium fluoride on hydrogenation properties of magnesium hydride. *Energies* **2015**, *8*, 12546–12556. [CrossRef]

27. Rönnebro, E.C.E.; Whyatt, G.; Powell, M.; Westman, M.; Zheng, F.; Fang, Z.Z. Metal hydrides for high-temperature power generation. *Energies* **2015**, *8*, 8406–8430. [CrossRef]

28. Cao, Z.; Ouyang, L.; Wang, H.; Liu, J.; Sun, L.; Felderhoff, M.; Zhu, M. Development of Zr-Fe-V alloys for hybrid hydrogen storage system. *Int. J. Hydrogen Energy* **2016**, *41*, 11242–11253. [CrossRef]

29. Lushnikov, S.A.; Movlaev, E.A.; Bobrikov, I.A.; Simkin, V.G.; Verbetsky, V.N. Hydriding of TiMo alloys at high hydrogen pressures. *Inorg. Mater.* **2016**, *52*, 1126–1131. [CrossRef]

30. Ulmer, U.; Dieterich, M.; Pohl, A.; Dittmeyer, R.; Linder, M.; Fichtner, M. Study of the structural, thermodynamic and cyclic effects of vanadium and titanium substitution in laves-phase AB2 hydrogen storage alloys. *Int. J. Hydrogen Energy* **2017**, *42*, 20103–20110. [CrossRef]

31. Takeichi, N.; Senoh, H.; Takeshita, H.T.; Oishi, T.; Tanaka, H.; Kiyobayashi, T.; Kuriyama, N. Hydrogenation properties and structure of Ti-Cr alloy prepared by mechanical grinding. *Mater. Sci. Eng. B Solid-State Mater. Adv. Technol.* **2004**, *108*, 100–104. [CrossRef]

32. Puszkiel, J.; Garroni, S.; Milanese, C.; Gennari, F.; Klassen, T.; Dornheim, M.; Pistidda, C. Tetrahydroborates: Development and potential as hydrogen storage medium. *Inorganics* **2017**, *5*, 74. [CrossRef]

33. Møller, K.T.; Sheppard, D.; Ravnsbæk, D.B.; Buckley, C.E.; Akiba, E.; Li, H.W.; Jensen, T.R. Complex metal hydrides for hydrogen, thermal and electrochemical energy storage. *Energies* **2017**, *10*, 1645. [CrossRef]

34. Yao, Z.; Liu, L.; Xiao, X.; Wang, C.; Jiang, L.; Chen, L. Effect of rare earth doping on the hydrogen storage performance of Ti1.02Cr1.1Mn0.3Fe0.6 alloy for hybrid hydrogen storage application. *J. Alloys Compd.* **2018**, *731*, 524–530. [CrossRef]

35. Bibienne, T.; Gosselin, C.; Bobet, J.L.; Huot, J. Replacement of vanadium by ferrovanadium in a Ti-based Body Centred Cubic (BCC) alloy: Towards a low-cost hydrogen storage material. *Appl. Sci.* **2018**, *8*, 1151. [CrossRef]

36.　Li, B.; Li, J.; Shao, H.; Li, W.; Lin, H. Synthesis, morphology, and hydrogen absorption properties of TiVMn and TiCrMn nanoalloys with a FCC structure. *Scanning* **2018**, *2018*, 1–10. [CrossRef] [PubMed]

37.　Milanese, C.; Garroni, S.; Gennari, F.; Marini, A.; Klassen, T.; Dornheim, M.; Pistidda, C. Solid state hydrogen storage in alanates and alanate-based compounds: A review. *Metals (Basel)* **2018**, *8*, 567. [CrossRef]

38.　Garroni, S.; Santoru, A.; Cao, H.; Dornheim, M.; Klassen, T.; Milanese, C.; Gennari, F.; Pistidda, C. Recent progress and new perspectives on metal amide and imide systems for solid-state hydrogen storage. *Energies* **2018**, *11*, 1027. [CrossRef]

39.　Jepsen, J.; Milanese, C.; Puszkiel, J.; Girella, A.; Schiavo, B.; Lozano, G.A.; Capurso, G.; Von Colbe, J.M.B.; Marini, A.; Kabelac, S.; et al. Fundamental material properties of the 2LiBH4-MgH2 reactive hydride composite for hydrogen storage: (I) Thermodynamic and heat transfer properties. *Energies* **2018**, *11*, 1081. [CrossRef]

40.　Jepsen, J.; Milanese, C.; Puszkiel, J.; Girella, A.; Schiavo, B.; Lozano, G.A.G.A.; Capurso, G.; Bellosta von Colbe, J.M.; Marini, A.; Kabelac, S.; et al. Fundamental material properties of the 2LiBH4-MgH2 reactive hydride composite for hydrogen storage: (II) Kinetic properties. *Energies* **2018**, *11*, 1170. [CrossRef]

41.　Li, J.; Jiang, X.; Li, G.; Li, X. Development of Ti1.02Cr2-x-yFexMny (0.6 ≤ x ≤ 0.75, y = 0.25, 0.3)alloys for high hydrogen pressure metal hydride system. *Int. J. Hydrogen Energy* **2019**, *44*, 15087–15099. [CrossRef]

42.　Kandavel, M.; Ramaprabhu, S. Hydriding properties of Ti-substituted non-stoichiometric AB2 alloys. *J. Alloys Compd.* **2004**, *381*, 140–150. [CrossRef]

43.　Nyamsi, S.N.; Tolj, I.; Lototskyy, M. Metal hydride beds-phase change materials: Dual mode thermal energy storage for medium-high temperature industrialwaste heat recovery. *Energies* **2019**, *12*, 3949. [CrossRef]

44.　Dematteis, E.M.; Baricco, M. Hydrogen desorption in Mg(BH4)2-Ca(BH4)2 system. *Energies* **2019**, *12*, 3230. [CrossRef]

45.　Li, J.; Jiang, X.; Li, Z.; Jiang, L.; Li, X. High-pressure hydrogen storage properties of TixCr1—yFeyMn1.0 alloys. *Int. J. Energy Res.* **2019**, *43*, 5759–5774. [CrossRef]

46.　Wang, Q.; Dai, X.; Wu, C.; Mao, Y.; Chen, Y.; Cao, X.; Yan, Y.; Wang, Y.; Zhang, H. Lattice defects and micro-strains in V60Ti25Cr3Fe12 alloy and influence on the ab/desorption of hydrogen. *J. Alloys Compd.* **2020**, *830*, 154675. [CrossRef]

47.　Puszkiel, J.; Gasnier, A.; Amica, G.; Gennari, F. Tuning LiBH4 for hydrogen storage: Destabilization, additive, and nanoconfinement approaches. *Molecules* **2020**, *25*, 163. [CrossRef] [PubMed]

48.　Kojima, Y.; Kawai, Y.; Towata, S.; Matsunaga, T.; Shinozawa, T.; Kimbara, M. Development of metal hydride with high dissociation pressure. *J. Alloys Compd.* **2006**, *419*, 256–261. [CrossRef]

49.　Mitrokhin, S.; Zotov, T.; Movlaev, E.; Verbetsky, V. Synthesis and properties of AB5-type hydrides at elevated pressures. *J. Alloys Compd.* **2007**, *446–447*, 603–605. [CrossRef]

50.　Shibuya, M.; Nakamura, J.; Akiba, E. Hydrogenation properties and microstructure of Ti-Mn-based alloys for hybrid hydrogen storage vessel. *J. Alloys Compd.* **2008**, *466*, 558–562. [CrossRef]

51.　Zotov, T.; Movlaev, E.; Mitrokhin, S.; Verbetsky, V. Interaction in (Ti,Sc)Fe2-H2 and (Zr,Sc)Fe2-H2 systems. *J. Alloys Compd.* **2008**, *459*, 220–224. [CrossRef]

52.　Shibuya, M.; Nakamura, J.; Enoki, H.; Akiba, E. High-pressure hydrogenation properties of Ti-V-Mn alloy for hybrid hydrogen storage vessel. *J. Alloys Compd.* **2009**, *475*, 543–545. [CrossRef]

53.　Takeichi, N.; Senoh, H.; Yokota, T.; Tsuruta, H.; Hamada, K.; Takeshita, H.T.; Tanaka, H.; Kiyobayashi, T.; Takano, T.; Kuriyama, N. "Hybrid hydrogen storage vessel", a novel high-pressure hydrogen storage vessel combined with hydrogen storage material. *Int. J. Hydrogen Energy* **2003**, *28*, 1121–1129. [CrossRef]

54.　Mori, D.; Hirose, K. Recent challenges of hydrogen storage technologies for fuel cell vehicles. *Int. J. Hydrogen Energy* **2009**, *34*, 4569–4574. [CrossRef]

55.　Matsunaga, T.; Shinozawa, T.; Washio, K.; Mori, D.; Ishikikiyama, M. Development of metal hydrides for high pressure mh tank. *Mater. Issues Hydrogen Econ.* **2009**, 144–154. [CrossRef]

56.　Mori, D.; Haraikawa, N.; Kobayashi, N.; Kubo, H.; Toh, K.; Tsuzuki, M.; Shinozawa, T.; Matsunaga, T. High-pressure metal hydride tank for fuel cell vehicles. *SAE Tech.* **2005**, *884*, 72–78. [CrossRef]

57.　Chengdu Huarui Industrial Co., Ltd. Available online: https://hrmetal01.en.alibaba.com/?spm=a2700.details. cordpanyb.4.62706069FtdeVg (accessed on 30 April 2020).

58. Izumi, F. Rietveld analysis and MEM-based whole-pattern fitting under partial profile relaxation. *Rigaku J.* **2000**, *17*, 34–35.

59. Jepsen, J. *Technical and Economic Evaluation of Hydrogen Storage Systems Based on Light Metal Hydrides*; HZG Report 2014-2; Helmut-Schmidt-University: Hamburg, Germany, 2014.

60. Hemmes, H.A.; Driessen, R.G. Thermodynamic properties of hydrogen at pressures up to 1 Mbar and temperatures between 100 and 1000K. *J. Phys. C Solid State Phys.* **1986**, *19*, 3571–3585. [CrossRef]

61. Puszkiel, J.A. *Preparation, Study and Optimization of Complex Hydrides for Hydrogen Storage (in Spanish)*; Universidad Nacional de Cuyo, Instituto Balseiro: San Carlos de Bariloche, Río Negro, Spain, 2012.

62. Schulz, R.; Huot, J.; Boily, S. Equipment for Gas Titration and Cycling of an Absorbent or Adsorbent Material. Pantent CA2207149A1, 10 February 2009.

63. Lozano, G.A.; Ranong, C.N.; Bellosta von Colbe, J.M.; Bormann, R.; Hapke, J.; Fieg, G.; Klassen, T.; Dornheim, M. Optimization of hydrogen storage tubular tanks based on light weight hydrides. *Int. J. Hydrogen Energy* **2012**, *37*, 2825–2834. [CrossRef]

64. Sánchez, A.R.; Klein, H.P.; Groll, M. Expanded graphite as heat transfer matrix in metal hydride beds. *Int. J. Hydrogen Energy* **2003**, *28*, 515–527.

65. Heubner, F.; Pohlmann, C.; Mauermann, S.; Kieback, B.; Röntzsch, L. Mechanical stresses originating from metal hydride composites during cyclic hydrogenation. *Int. J. Hydrogen Energy* **2015**, *40*, 10123–10130. [CrossRef]

66. Ge, H.-W.; Wang, X.-H.; Zhang, Y.; Li, H.; Chen, L.-X.; Li, S.-Q.; Yan, M.; Chen, C.-P. Hydrogen storage properties of Ti-Cr-Mn-M (M = V, Fe, Ni, Cu) alloys. *J. Funct. Mater.* **2009**, *40*, 420–423.

67. Standard ISO/DIS 15869.2:2006. *Gaseous Hydrogen and Hydrogen Blends—Land Vehicle Fuel Tanks—Part 2: Particular Requirements for Metal Tanks*; ISO: Geneva, Switzerland, 2006.

68. ZAO, Association of Aerospace Engineers. *Pionerskay 4 141070 KOROLEV MOSCOW REGION RUSSISCHE FÖDERATION*. Available online: https://unitech-mo.ru/eng/university/history/ (accessed on 30 April 2020).

69. Lundin, C.E.; Lynch, F.E.; Magee, C.B. A correlation between the interstitial hole sizes in intermetallic compounds and the thermodynamic properties of the hydrides formed from those compounds. *J. Less Common Met.* **1977**, *56*, 19–37. [CrossRef]

70. Beeri, O.; Cohen, D.; Gavra, Z.; Johnson, J.R.; Mintz, M.H. Thermodynamic characterization and statistical thermodynamics of the TiCrMn-H2(D2) system. *J. Alloys Compd.* **2000**, *299*, 217–226. [CrossRef]

71. Pickering, L.; Lototskyy, M.V.; Davids, M.W.; Sita, C.; Linkov, V. Induction melted AB2-Type metal hydrides for hydrogen storage and compression applications. *Mater. Today Proc.* **2018**, *5*, 10470–10478. [CrossRef]

72. Park, J.G.; Jang, H.Y.; Han, S.C.; Lee, P.S.; Lee, J.Y. The thermodynamic properties of Ti-Zr-Cr-Mn Laves phase alloys. *J. Alloys Compd.* **2001**, *325*, 293–298. [CrossRef]

73. Kittel, C. *Introduction to Solid State Physics*, 7th ed.; John Wiley & Sons: New York, NY, USA, 2020.

74. Somo, S.; Maponya, M.; Davids, D.; Hato, H.; Lototskyy, L.; Modibane, M. A Comprehensive Review on Hydrogen Absorption Behaviour of Metal Alloys Prepared through Mechanical Alloying. *Metals* **2020**, *10*, 562. [CrossRef]

75. Lototskyy, M.; Yartys, V.A. Comparative analysis of the efficiencies of hydrogen storage systems utilising solid state H storage materials. *J. Alloys Compd.* **2015**, *645*, S365–S373. [CrossRef]

76. U.S. Department of Energy Target Explanation Document: Onboard Hydrogen Storage for Light-Duty Fuel Cell Vehicles. In *U.S Drive*; 2017; pp. 1–29. Available online: https://www.energy.gov/eere/fuelcells/doe-technical-targets-onboard-hydrogen-storage-light-duty-vehicles (accessed on 30 April 2020).

77. Wriedt, H.A.; Oriani, R.A. Effect of tensile and compressive elastic stress on equilibrium hydrogen solubility in a solid. *Acta Met.* **1970**, *18*, 753–760. [CrossRef]

78. Nasako, K.; Ito, Y.; Hiro, N.; Osumi, M. Stress on a reaction vessel by the swelling of a hydrogen absorbing alloy. *J. Alloys Compd.* **1998**, *264*, 271–276. [CrossRef]

79. Davids, M.W.; Lototskyy, M.; Malinowski, M.; van Schalkwyk, D.; Parsons, A.; Pasupathi, S.; Swanepoel, D.; van Niekerk, T. Metal hydride hydrogen storage tank for light fuel cell vehicle. *Int. J. Hydrogen Energy* **2019**, *44*, 29263–29272. [CrossRef]

80. Available online: https://materialsproject.org/#search/materials (accessed on 30 April 2020).

81. Zheng, J.; Li, L.; Chen, R.; Xu, P.; Kai, F. High pressure steel storage vessels used in hydrogen refueling station. *J. Press. Vessel Technol.* **2008**, *130*, 244–254. [CrossRef]

82. NIST Reference Fluid Thermodynamic and Transport Properties Database (REFPROP): Version 8.0. Available online: http://www.nist.gov/srd/nist23.htm (accessed on 30 April 2020).